論文 / 著書情報
Article / Book Information

題目(和文)	
Title(English)	Optical interaction enhancement of MoS2 using nanostructures investigated by cathodoluminescence
著者(和文)	VuThi Dung
Author(English)	Dung Thi Vu
出典(和文)	学位:博士(工学), 学位授与機関:東京工業大学, 報告番号:甲第12199号, 授与年月日:2022年9月22日, 学位の種別:課程博士, 審査員:三宮 工,北本 仁孝,中辻 寛,和田 裕之,梶川 浩太郎
Citation(English)	Degree:Doctor (Engineering), Conferring organization: Tokyo Institute of Technology, Report number:甲第12199号, Conferred date:2022/9/22, Degree Type:Course doctor, Examiner:,,,,
学位種別(和文)	博士論文
Type(English)	Doctoral Thesis

東京工業大学
Tokyo Institute of Technology

THESIS FOR THE DEGREE OF DOCTOR OF ENGINEERING

Optical interaction enhancement of MoS_2 using nanostructures investigated by cathodoluminescence

Dung Thi Vu

Department of Materials Science and Engineering

Tokyo Institute of Technology

Yokohama, Japan 2022

Acknowledgements

Firstly, I would like to express my sincere gratitude to my research supervisor, Professor Takumi Sannomiya, for giving me the opportunity to do research and providing invaluable guidance throughout this research. He teachs me the methodology to carry out the research and to present the research works as clearly as possible. It was a great privilege and honor to work and study under his guidance. Professor Sannomiya is not only an excellent researcher but also a great person who is always supportive and willing to help with any issue.

I would like to thank Professor Kotaro Kajikawa for recommending the IGP-A program in Tokyo Institute of Technology to me so that I have the opportunity to study and research here. In addition, he always answers my questions about the program and gives me valuable comments during the joint research presentations with his lab. I would like to thank my Professor Kitamoto Yoshitaka for being my sub-supervisor, and Professor Chai for always encouraging me. I would like to express my gratitude to the Tokyo Institute of Technology where I am provided valuable lessons from excellent teachers, and a research environment with the modern facility. I would like to thank the Japanese Ministry of Education, Culture, Sports, Science, and Technology for offering me the MEXT scholarship and supporting me for 5 years.

I would like to thank my parents, Mr. Vu Tri The and Ms. Nguyen Thi To, as well as my sister Ms. Vu Thi Duyen for their never-ending support and care. Without them, I probably wouldn't have been able to complete a small part of my journey.

Finally, I would also like to acknowledge Dr. Nguyen Ngoc Anh, Dr. Hoang Nam Hai, Dr. Nguyen Thi Thanh Hoa, Ms. Nguyen Thi Minh Chau, Ms. Nguyen Thi Bich Ngoc, Dr. Taeko Matsukata, Ms. Izzah Machfuudzoh, Mr. Yanagimoto Sotatsu, Mr. Aidachi Yoshikazu, Mr. Ogura Shintaro, and especially Mr. Homma Masahiro for their valuable friendship and for the great moments we share together about the work and the life.

Abstract

Plasmonic nanostructures can strongly confine the electromagnetic field, which enhances the interaction of light with materials. Molybdenum disulfide (MoS_2) possesses a great photoresponsivity for optoelectronic devices, however, it retains only a weak interaction with light especially for two-dimensional thin layers. In this thesis, two methods to enhance MoS_2 luminescence through optical interaction with nanostructures are presented and the enhancement is nanoscopically visualized. We fabricate and investigate plasmonic nanoholes and nanopyramids, using colloidal lithography and apply a cathodoluminescence (CL) technique to observe the locally enhanced emission from MoS_2. A significant luminescence enhancement in MoS_2 through a plasmonic-exciton coupling with a nanopyramid array is successfully demonstrated. Secondly, due to the high refractive index, light emission from MoS_2 nanoflake includes both exciton and dielectric resonances. We visualize the coupled exciton and dielectric modes experimentally and theoretically elucidate the experimental results.

Plasmonic nanohole arrays can efficiently enhance and concentrate the electromagnetic field via surface plasmon polaritons. The optical resonances in nanohole arrays are usually determined by the inter-hole spacing or periodicity with respect to the surface plasmon wavelength. However, because the inter-hole spacing varies locally in SRO arrays, the plasmon resonance fluctuates. Using the CL method, we investigate the local resonance of SRO nanoholes and compare to hexagonally ordered nanoholes. The CL photon maps and resonance peak analysis demonstrated that electric fields are localized at the edges of holes and that their resonances are influenced by inter-hole distances as well as their distributions. This illustrates Anderson localization of electromagnetic waves with regionally improved electromagnetic local density of states in SRO nanoholes. However, SRO nanoholes are not an ideal structure for optically coupling with MoS_2, because the plasmon

resonance wavelengths are not identical for every hole as well as the electric field intensity is not uniform, while exciton emission energies are fixed at 1.84 eV (A-exciton) and 2.03 eV (B-exciton). Therefore, in the next step, we fabricate and investigate the optical properties of periodic plasmonic nanopyramids, and then pair them with MoS_2 flakes.

The first method to enhance the emission intensity of MoS_2 reported in this thesis is through a hybrid structure consisting of MoS_2 flakes placed on top of the honeycomb nanopyramid array. To maximize the coupling efficiency, the plasmonic resonance of the nanopyramid array needs to be tuned by controlling its structure and materials to overlap with the excitonic peaks of the MoS_2 flake. Nanopyramid arrays are fabricated using colloidal lithography combined with a self-assembly technique. The local plasmonic field confined within the nanopyramids interacting with the excitons enhances the luminescence intensity of the MoS_2 flake. We experimentally visualized local luminescence enhancement in MoS_2 flakes in hybrid structures through CL map photons. By comparing the intensity of the MoS_2 emission with and without the underlying nanopyramids, we have successfully demonstrated a significant luminescence enhancement resulting from the plasmon-exciton coupling of Au nanopyramids and MoS_2 flakes.

MoS_2 are high refractive index materials that, when shaped into nanostructures, can effectively confine the electromagnetic field at nanoscale dimensions, resulting in complex light emission with exciton and dielectric resonances. In the second method of this thesis, we investigate the luminescence enhancement of MoS_2 caused by dielectric resonances in nanoscale dimensions by experimentally visualizing the emission modes of single MoS_2 nanoflakes. We observed dielectric modes with resonant wavelengths that fluctuate with the shape and size of the nanoflake, whereas the exciton emission peaks with energies are unaffected by flake geometry. We further theoretically and practically visualized the emission polarization and angular emission patterns using a fourth dimension CL (4D-CL) technique and boundary element

method (BEM) simulations. The acquired CL mapping indicates the interaction of the exciton and dielectric resonant modes, leading to field enhancement.

List of Abbreviations

AFM	Atomic force microscope
STEM	Scanning transmission electron microscopy
CL	Cathodoluminescence
MoS_2	Molybdenum disulfide
PS	Polystyrene
PMMA	Polymethyl methacrylate
ACH	Aluminum chlorohydrete
FEM	Finite element method
BEM	Boundary element method
BEI	Backscattered electron image
LSPR	Localized surface plasmon
SPPs	Surface plasmon polaritons
SRO	Short-range order
SPs	Surface plasmons

Contents

Chapter 1 - Introduction

1.1. Background

1.1.1. General introduction of this thesis

Surface plasmon polaritons (SPPs), which propagate at the interface between metal and dielectric, are formed by collective oscillation of free electrons[1]–[3]. Confinement of electromagnetic field via SPPs in nanoscale regions can be achieved by various nanostructures, such as nanoparticles, nanodisks, nanoholes and so on[4]–[6]. Strong field enhancement and optical field localization are believed to offer promising potential in applications such as plasmonic-integrated optical devices, photocatalysis, and solar cell conversion[7]–[10].

MoS_2 is one of the most common two-dimensional (2D) transition metal dichalcogenides (TMDCs)[11],[12], has received significant attention owing to its semiconductive nature, tunable bandgap, and its strong light-absorption capacity in the visible region. These characteristics enable its use in the development of semiconductor sensors[13], photocatalytic[14], hydrothermal and optoelectronic devices[12]. When the thickness of a bulk MoS_2 semiconductor is lowered to a monolayer, the indirect bandgap turns to a direct bandgap, leading in a remarkably greater luminescence than bulk MoS_2[15]. The TMDC family of materials possess high refractive indices and are capable of optical field confinement that can improve light-matter interactions based on the occurrence of dielectric cavity modes Such materials have a general formula of MX_2 (where M = Mo, W; X = S, Se, Te) [14]–[21].

However, luminescence quantum efficiency of MoS_2 layer-structures is usually weak, due to a low light absorption, preventing deployment into the applications. There have been significant efforts to enhance the MoS_2 luminescence in the past. Among them, hybrid structures consisting of the MoS_2 semiconductors and plasmonic nanoparticles have been considered a great platform for luminescence enhancement due to an exciton-plasmon coupling. For example, recently the optical response of

MoS_2 in the MoS_2-Ag hybrid nanostructures under illumination by the laser has been studied. As the result, the MoS_2 exciton emission is enhanced significantly due to the local fields at the position of the emitters arising from the LSPR of Ag disks. The emission enhancement results from the optical interaction in the system consisting of the plasmon field and the dipole excitons, leading to an enhancement in both the excitation rate as well as the enhanced emission rate via the Purcell effect [22]–[25]. In addition to plasmonic nanostructures, the emission-enhanced interaction of MoS_2 based on the local electromagnetic effect can also be achieved through dielectric nanoparticles, which are related to Mie resonance.

Mie resonances in high-index dielectric nanoparticles allow for the confinement of electromagnetic fields at the nanoscale which are sensitive to geometrical characteristics of the particle[23]. Dielectric resonant wavelength of such particles is sensitive to the size, the shape and to it surrounding environment. MoS_2 is a semiconductor material with a high refractive index, resulting a complex light emission in MoS_2 nanoflakes, including the intrinsic luminescence and dielectric resonant modes that emit light in the visible spectral range. Visualization of the optical characteristics beyond the diffraction limit of light is necessary to determine the mechanisms behind the multiple emission, to examine the origin of the nanoscopic optical features of the MoS_2 nanoflake. This is accomplished by utilizing an electron beam as a high-energy and high-momentum excitation source with a size of down to 1 nm, resulting in the excitation of all electron transitions in the material with nanoscale precision, which PL spectroscopy usually does not allow[26], [27]. This type of nanoscopic observation provides a detailed knowledge on the optical response of MoS_2, including enhanced coupling of excitons and dielectric resonances, which are important in the development of MoS_2-based optoelectronic devices.

1.1.2. Current status of luminescence enhancement in MoS_2

Because A- and B-exciton emissions of monolayer MoS_2 has direct bandgaps with absorption in the visible region of the spectrum, as well as many other excellent

properties well suitable for optoelectronic applications, including high extinction coefficients, remarkable mechanical properties, and chemical and physical stability, it has opened new interesting possibilities in optoelectronic devices[28]–[30]. MoS_2 thin layers, on the other hand, frequently show low photoluminescence quantum yields (PLQYs), which is the essential figure of merit for optoelectronic devices[31]. There have been significant efforts to enhance the MoS_2 luminescence in the past, including chemical treatments and physical assistances[23].

Chemical treatments

Sulfur vacancies are the predominant type of defect in the crystal structure of MoS_2 which is the main cause of several nonradiative recombination processes that lead to a decrease in PL intensity in MoS_2. Many reports indicate that it is possible to enhance the luminescence intensity of MoS_2 by treating the defect spots by treating it with some suitable chemicals. These chemicals have been studied and reported as hydrogen peroxide, oxygen, and superacid[32]. Several studies have demonstrated bis(trifluoromethane)-sulfonimide (TFSI) can be filled with sulfur vacancies in MoS_2 in order to enhance the emission intensity. In addition, TFSI is also considered as an effective method for improving the emissivity of other TMDs such as MoS_2, WS_2, $MoSe_2$, and WSe_2. However, because TFSI is an extremely strong acid, its harsh properties can cause damage to MoS_2 materials, its contacts in optoelectronic devices, and thus limit the application of MoS_2[33][32][31]. A method that combines both chemical and physical methods to enhance the luminescence intensity of monolayer MoS_2 has been realized by Christian.S et al.[33], by utilizing the confined electromagnetic field from arrays of monolayer Au plasmonic particles and at the same time, chemically treating the surface of the MoS_2 layer with TFSI super acid. The obtained emission intensity is increased up to a few hundred times which is promising for the development of MoS_2-based optoelectronic devices.

Physical assistance

Different from the chemical processing methods described above, physical methods make use of the local electronic fields obtained by nanomaterial structures which do not requires harsh chemicals. The nanostructures can be plasmonic, dielectric, or hybrid structures specifically designed to accommodate optical coupling with MoS_2, for maximum enhanced performance. It has been reported in several studies that plasmonics, photonic cavities, and, optical waveguides, have been considered for emission-enhanced coupling with MoS_2 layer structure[34]. Among optical nanostructures, plasmonics is considered a great platform to enhance light-matter interactions, thus a high potential for applications for photonic devices, due to the electromagnetic modes induced by plasmon resonance. These electromagnetic fields are known as LSPR modes that are confined from nanostructures such as nanoparticles, nanodisks, nanorods, and so on to produce "hot-spots" with a relatively high electric field strength, for effective optical interaction with the excitons of MoS_2. These fields localized into the nanostructures can be tuned for resonant frequency, polarization or other optical properties by controlling the shape, size structure, material, or environment. its surroundings[23]. However, for these nanometer-sized structures, making and manipulating them on a large scale with a simple, effective, and inexpensive method has always been considered a major challenge.

1.1.4. Nanoholes fabrication

Since widely used techniques like focused ion beam or electron beam lithography are serial procedures, they are time- and money-consuming, making it difficult to fabricate periodic nanohole arrays over large surfaces. Using a less complex method based on colloidal self-assembly, hexagonal periodicity nanoholes have been fabricated. However, due to the unexpected positions of the colloids on the surface and the domain formations, this method seems unable to perfectly arrange the holes of a single crystal[36]. Another solution is the SRO nanohole array, which can be readily and quickly produced on millimeter scales using the colloidal lithography technique.

The SRO nanoholes include randomly distributed holes that comply with a characteristic spacing between holes[37].

1.1.3. Current status of nanostructure fabrication

Nanolithography is a process of imprinting, writing or etching patterns at the micro/nano level to create small structures commonly used to create electronic devices with smaller sizes and faster speeds. Some nanolithography techniques used commonly are lithography techniques using X-ray, electron-beam direct-write and extreme ultraviolet, and colloidal lithography technique. Nowadays, scientists and engineers can manufacture nanostructures at unprecedented sizes, precision, and throughput using methods like as electron-beam lithography, focused-ion-beam lithography, optical lithography, nanoimprint, nano-molding, and scanning-probe lithography. Some of the most often utilized approaches are presented below.

- **Focused ion beam lithography (FIBL)**

FIBL is a technique that allow directly writing nanoscale patterns on substrates, applied in nanofabrication such as resist exposure, etching, milling, using high-energy focused ion beams. Regarding the ion source used for FIBL, the most used gallium ion is suitable for the fabrication of structures about 20 nm in size. Currently, helium sources have been used with the outstanding advantage of being able to create structures with microscopic sizes of less than 10 nm. Since helium IBL has a lower mass than gallium IBL, it has a lower sputtering rate, suitable for plasmonic antennas or graphene with nanostructures with sizes as low as 3 nm. Because the mass of the Gallium ions is heavier than that of photons or electrons, ion beam lithography generally has the capacity to offer greater resolution than photolithography and electron beam lithography. Due to the short wavelength of ions, there is relatively little particle diffraction or scattering. The primary or secondary electrons are strongly diffracted and scattered since there is no necessity for specially designed resistors to be employed in electron-beam lithography. Ion beam lithography, however, mandates the

use of thinner resistive layers than electron beam or optical lithography because to the limited penetration depth of ions into substrate[38].

- **Electron beam lithography (EBL)**

Electron beam lithography (EBL) is a direct writing technology that does not require a photomask and may produce smaller features than optical lithography because to the significantly shorter wavelength of the electron beam[39]. Poly(methyl methacrylate) and hydrogen silsesquioxane are used as typical positive and negative resists, respectively, to write nanoscale patterns on an e-beam sensitive resist deposited on a target substrate. The correct resist/developer selection and meticulous post-exposure manufacturing technique are critical for producing well-defined nanostructures. EBL-facilitated nanostructures have been created using a variety of materials. However, EBL's scalability is restricted because it is often utilized as photomasks, striped templates, or nano-imprinted molds[40].

- **Colloidal lithography**

Colloidal lithography technique combines bottom-up and top-down methods, which is also a resist-free nanofabrication technology. Colloidal lithography manufacturing requires establishing a monolayer on a substrate with manufactured nanospheres. Following the formation of a closed-packed monolayer, the substrate layer is subjected to plasma generating techniques to minimize colloidal sizes, followed by metal deposition[40]. For example, employing O_2 plasma treatment, hexagonal nanoholes with diameters of (a) 156 nm, (b) 210 nm, and (c) 238 nm have been effectively controlled by lowering the size of colloidal nanoparticles to 320 nm[36]. Although this technology is inexpensive, it is limited by the time-consuming particle patterning stages and the imperfect arrangement of the colloidal pack.

1.1.4. Purpose of thesis

In this thesis, we present two methods to enhance MoS_2 luminescence through optical interaction with nanostructures and the enhancement is nanoscopically visualized. We fabricate and investigate plasmonic nanoholes and nanopyramids, using colloidal lithography. The scanning transmission electron microscope-cathodoluminescence (STEM-CL) method is used for the measurement of the optical characteristics of nanostructures with a narrow excitation about 1 nm. The CL method enables electromagnetic local density of states (EMLDOS) mapping with high spatial resolution measurement allowing parameters such as field distribution at a certain energy, polarization, and emission angle of structures at the nanoscale.

Firstly, the SRO plasmonic nanoholes with random hole distribution are fabricated by a combination of colloidal lithography techniques which is a simple but effective method. Field localization of SRO nanoholes which depends on the hole-to-hole distance is evaluated.

For the first method, to achieve luminescence enhancement of MoS_2, it requires a suitable design of the plasmonic structure for matching the plasmonic resonance range with exciton emission energy. The enhancement is evaluated through the CL photon maps which allows visualization of optical modes and the local enhancement.

For the second method, the exciton and dielectric modes coexist in single MoS_2 nanoflakes. The geometry dependence of dielectric mode and its optical interaction with excitons is investigated in nanoscale.

1.1.5. Structure of thesis

This thesis presents information on the optical interaction enhancement of MoS_2 semiconductor using nanostructures investigated by CL technique. The thesis is separated into three main chapters excluding introduction, methods, and conclusion: "

Short-range order plasmonic nanoholes" (Chapter 3), "Exciton-dielectric mode coupling of single MoS_2 nanoflakes " (Chapter 4) and “Luminescence enhancement of MoS_2 flake through plasmonic-exciton coupling (Chapter 5). The structure is shown in the chart of Figure 1.1

The outline of each chapter is described below.

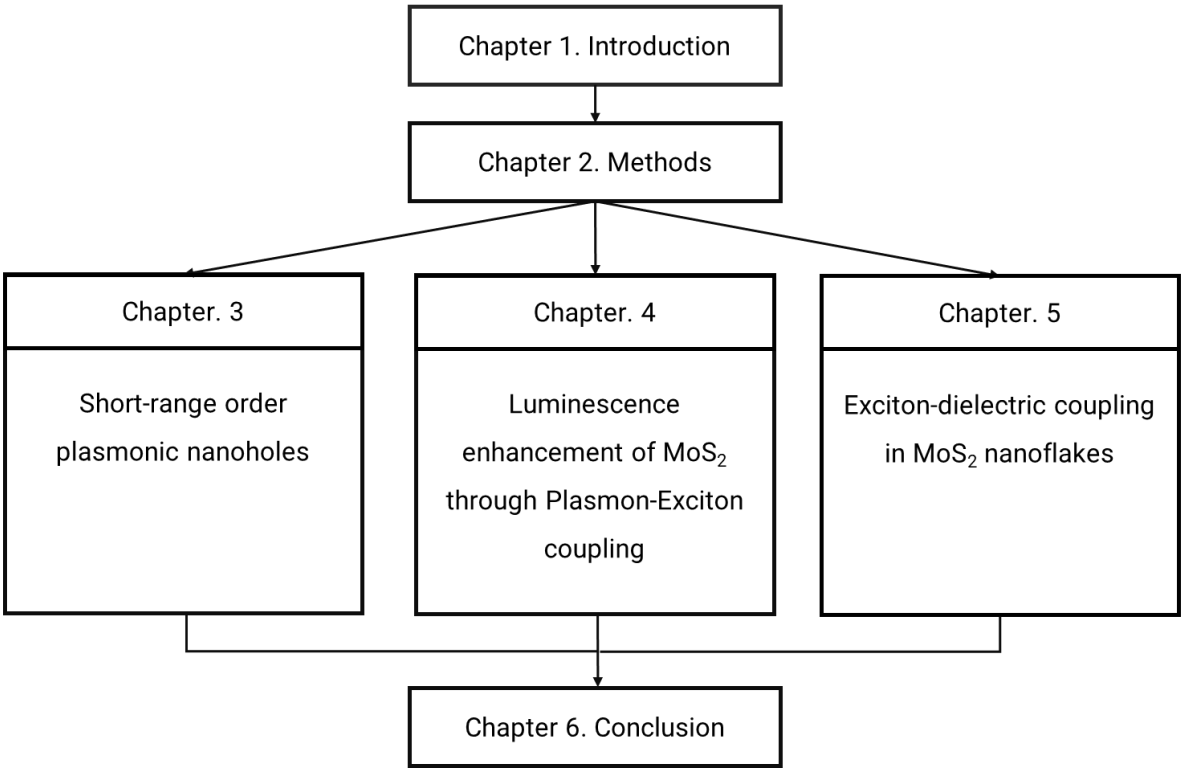

Figure 1.1. Thesis structure

Chapter 1: Firstly, we introduce general about surface plasmon and MoS_2 semiconductor material. The luminescence of MoS_2 semiconductors is still weak for applications which requires efficient methods to solve this problem. Therefore, we present potential methods using optical nanostructures used in this thesis. this. The current research status of MoS_2 luminescence enhancement and fabrication of nanostructures, purpose and structures of this thesis are presented.

Chapter 2: We present the methods used in this thesis. We introduce the method of magnetic sputtering deposition, STEM and AFM devices. In addition, CL methods and CL types are classified according to the emission mechanism.

Chapter 3: Colloidal lithography and a thin film transfer technique with a self-assembled colloid mask layer are used to produce short-range ordered (SRO) nanoholes on the Au membrane. The optical characteristics of SRO nanoholes are investigated using CL and transmission spectra. The optical characteristics of SRO holes are compared to hexagonal holes to highlight the effect of hole arrangement on plasmon resonances. Through CL mapping, we reveal the Anderson localization of electromagnetic waves in SRO plasmonic nanoholes. Spectral peak analysis is used to assess the spatial distribution of the resonance and intensity of the spectrum.

Chapter 4: In this chapter, we present the first method to enhance the internal luminescence using a hybrid structure consisting of MoS_2 flake placed on top of Au nanopyramid arrays. To achieve the luminescence enhancement in MoS_2, it requires a suitable design and optical controls for Au plasmonic nanopyramid structure, to maximize the coupling efficiency with the excitons of MoS_2. The Au nanopyramid array is fabricated using a combination of colloidal lithography and self-assembly techniques of the particles. Using the 4D-CL technique allowed us to obtain momentum resolution patterns at the exciting beam positions and extract photon energy maps at all radiation angles from the arrays. Finally, the enhanced local emission of MoS_2 is successfully demonstrated to map the CL electric field distribution by the interaction with the local electric field provided by the Au plasmonic pyramid.

Chapter 5: Using a STEM-CL system, we visualize emission processes supported in individual MoS_2 nanoflakes via CL mapping. The photon emission distribution on individual nanoflakes is mapped, followed by a comparison of emission wavelengths for various flake shapes. The acquired CL mapping data is spectrally deconvoluted to split the overlapping emission modes in nanoflake, and the dielectric mode is

determined further based on the field distribution. We explore how the resonant modes contribute to luminescence enhancement based on the identified deconvoluted peaks. Moreover, because measured CL signals are superpositions of various emission modes, we use the 4D-CL approach to determine the angular spectrum at stimulated beam points and extract photon energy maps from the flake in all radiation angles.

Chapter 6: Conclusion of the thesis and outlook.

1.2. Principle

1.2.1. Surface plasmon polaritons

SPRs are electromagnetic waves traveling along the interface of a dielectric/metal or air/metal. The interface is mainly a combination of positive and negative permitting materials. Positive permitting materials, commonly known as dielectric materials, such as air or glass. Negative permitting materials are metals that contain free electrons such as Au, Cu, Ag, etc. To investigate the SPP physical characteristic, Maxwell equations are used to apply a planar interface of a metal and a dielectric[41]. By solving these equations with the boundary conditions, the dispersion relation for a surface propagating wave is:

$$K_{SP} = K_o \left(\frac{\varepsilon d \varepsilon m}{\varepsilon d + \varepsilon m}\right)^{1/2}$$

In which: K_{SP} is the SP wave vector; c is the speed of light; $K_o = \frac{\omega}{c}$ free space photon wave vector. The condition for SPs to propagate along the dielectric/metal interface, the permittivity of the conducting surface ε_m, and the dielectric medium, ε_d have opposite signs.

1.2.2. Diffraction grating

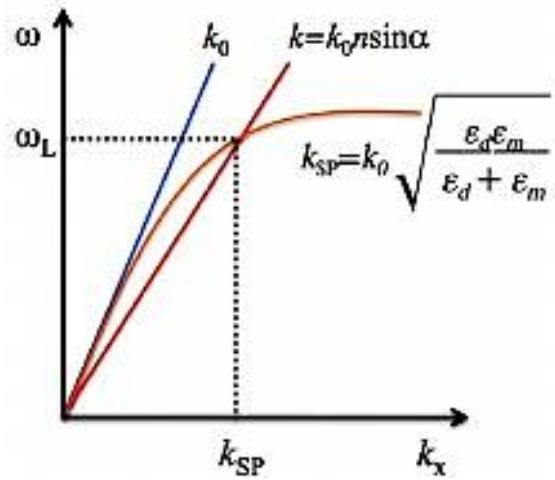

Figure 1.2. Dispersion curve for a surface plasmon mode shows the wave vector mismatch problem between incident light in blue line and SP modes in orange curve. The wave-vector of incident light is shifted by using evanescent wave created by using several methods such as prism setups or diffraction gratings (in the red line)[42].

Figure 1.2. presents the dispersion curve of a surface plasmon mode. It can be seen in the figure that at the same frequency, the positions of the surface plasmon mode line and the light line are different, which means there is a mismatch problem of wave vectors. The mismatch in wave vector between the in-plane momentum of impinging photons and propagating constant can be overcome by patterning the metal surface with a grating of grooves or holes with lattice constant $\boldsymbol{a}$. For the simple one-dimensional grating of grooves depicted in Figure 1.3. Firstly, it is defined that SPPs propagate along with the x-direction, and the wave vectors of incident light and the diffracted light are also defined as $\boldsymbol{k}$ and $\boldsymbol{k}'$, respectively. In addition, all angles (θ, φ, and φ') are defined in Figure 1.3.

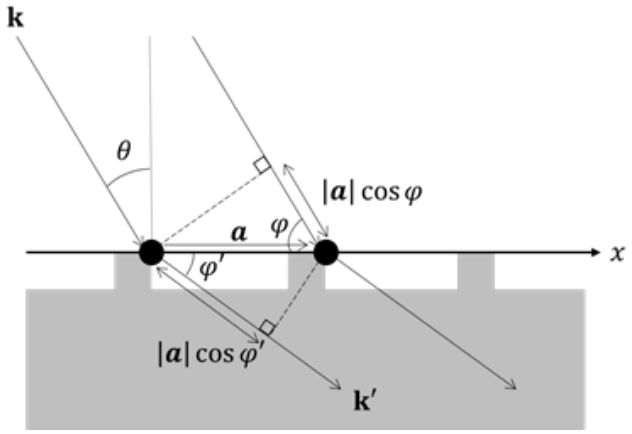

Figure 1.3. A schematic illustration of a diffraction at the metal grating's surface.

$$\boldsymbol{k} = \frac{2\pi}{\lambda}\boldsymbol{n}$$

$$\boldsymbol{k}' = \frac{2\pi}{\lambda}\boldsymbol{n}'$$

where λ is the wavelength, and $\boldsymbol{n}$ and $\boldsymbol{n}'$ are the unit vector, respectively. The x-components of wave vector of incident light (k_x) is given as:

$$k_x = \boldsymbol{k}\sin\theta \qquad \text{(E.q. 1)}$$

When the lattice vector of the metal grating is $\boldsymbol{a}$, the reciprocal vector of the grating ($\boldsymbol{g}$) is given as:

$$\boldsymbol{g} = \frac{2\pi}{\boldsymbol{a}} \qquad \text{(E.q. 2)}$$

The constructive condition is given as:

$$|\boldsymbol{a}|(\cos\varphi' - \cos\varphi) = \pm v\lambda \qquad \text{(E.q. 3)}$$

where $v\ (= 1, 2, 3, \ldots)$ is positive integer. Using below equations of inner product,

$$\boldsymbol{a}\cdot\boldsymbol{n}' = |\boldsymbol{a}|\cos\varphi' \qquad \text{(E.q. 4)}$$

$$\boldsymbol{a}\cdot\boldsymbol{n} = |\boldsymbol{a}|\cos\varphi \qquad \text{(E.q. 5)}$$

the constructive condition can be modified through the following deformation:

$$\boldsymbol{a} \cdot (\boldsymbol{n}' - \boldsymbol{n}) = \pm v\lambda \quad \text{(E.q. 6)}$$

$$\frac{2\pi}{\lambda}(\boldsymbol{n}' - \boldsymbol{n}) = \pm v\frac{2\pi}{\boldsymbol{a}} \quad \text{(E.q. 7)}$$

$$\boldsymbol{k}' - \boldsymbol{k} = \pm v\boldsymbol{g} \quad \text{(E.q. 8)}$$

$$\boldsymbol{k}' = \boldsymbol{k} \pm v\boldsymbol{g} \quad \text{(E.q. 9)}$$

By considering the x-component of the diffracted light (k'_x) in (E.q. 84), one can obtain the following equation.

$$k'_x = |\boldsymbol{k}| \sin\theta \pm v|\boldsymbol{g}| \quad \text{(E.q. 10)}$$

If $k'_x = \beta$, SPPs can be excited. Therefore, the excitation condition of SPPs for the metal grating is given as:

$$\beta = |\boldsymbol{k}| \sin\theta \pm v|\boldsymbol{g}| \quad \text{(E.q. 11)}$$

If one rewrites this excitation condition as below,

$$\beta \mp v|\boldsymbol{g}| = |\boldsymbol{k}| \sin\theta \quad \text{(E.q. 12)}$$

this expression implies that the dispersion curve of SPPs can be shifted by the integral multiple of the reciprocal vector of the grating ($\boldsymbol{g}$).

Chapter 2- Methods

2.1. Magnetron sputtering

Sputtering is a thin film fabrication technique based on the principle of kinetic energy transfer by using noble gas ions such as Ar_2 or N_2 gas accelerated under an electric field to bombard the material surface of a target, thus, transfer kinetic energy to these atoms. Schematic illustration of the magnetron sputtering is presented in Figure 2.1[43]. Such atoms move towards to the substrate, then the layer of material will be deposited on the substrate. The sputtering technique is evaluated as one of the thin film techniques with excellent coverage and high uniformity. However, the low deposition rate is a drawback of this method. An improvement from conventional sputtering systems is thus produced by placing magnets underneath the target. The magnetic field of the magnet is used to trap electrons into the vicinity of the target to increase the ionization effect. This is achieved because the frequency of collisions between electrons and gas atoms near the target surface is enhanced, thus increasing the deposition rate. This method presents several important advantages over other vacuum coating techniques, which have led to the development of a large number of commercial applications ranging from microelectronic fabrication to decorative coatings. Outstanding advantages from magnetron sputtering can be mentioned such as high deposition rate, ease of splashing any metal, alloy or compound, high purity film, high film adhesion[43].

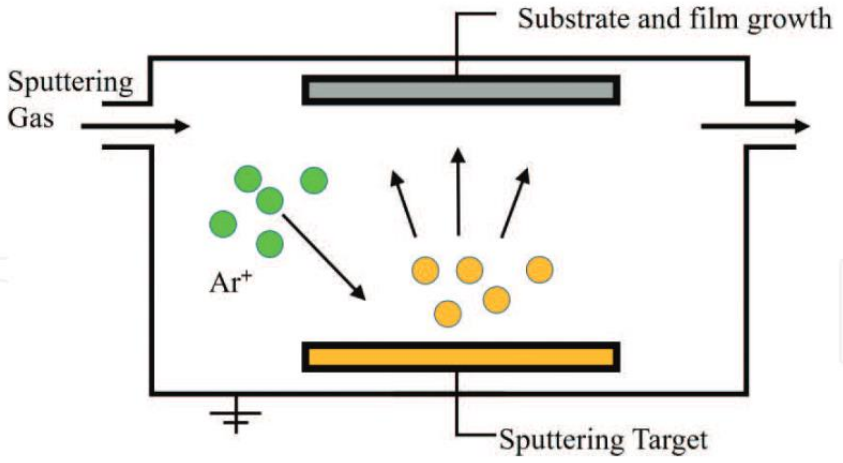

Figure 2.1: Schematic illustration of the magnetron sputtering.

2.3. Atomic force microscope

AFM was first developed in 1985 to overcome the disadvantage of Scanning Tunneling Microscopy technique that it can only be performed on conductive samples. AFM can image the surface of all types of samples including non-conductive samples and works even in normal environments, without requiring a high vacuum environment. In addition, AFM also works without the destruction of the specimen or the supply of electrical current, making it suitable for biological samples as well. However, this device also has some disadvantages such as only scanning images on a narrow area, with slow image recording speed due to operation in scan mode. Surface vibration transducers are less secure and require samples with clean surfaces and vibration resistance[44][43].

AFM is a device used to close the surface structure of solid objects based on the principle of determining the atomic force between a pointed probe tip and the surface of the sample, which can be observed at nanometer resolution. The pointed tip is mounted on a cantilever has the size of one atom. When the tip scan close to the surface of the specimen, the atom of the tip and the sample surface will appear Van der Waals forces that vibrate the cantilever. The oscillation due to this interaction force is immediately recorded by the angle change of a laser beam which is pointed to the cantilever, and finally recorded by the detector. The interaction force recorded during the vibrating rod scanning the surface will provide an image of the surface structure of the specimen. A schematic illustration of the AFM working principle is shown in Figure 2.2[45].

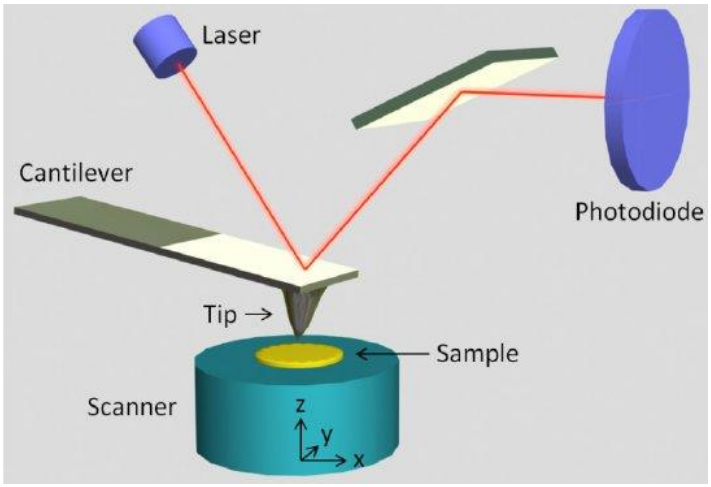

Figure 2.2. A schematic representation of the AFM operating principle[45].

2.4. Scanning transmission electron microscope

STEM is a type of transmission electron microscope in which an electron beam is focused into a single and very narrow beam, scanning over the sample surface when it passes through the sample. STEM is a transmission electron microscope offering a high resolution to the atomic scale and many useful analyzes associated with it. STEM is widely used in materials science for the purposes of observation, quality control, and structural and morphological analysis of materials. Especially for nanomaterial structures, STEM is used to describe the subatomic structure of materials, thereby providing important information about the properties and behavior of materials. In addition, STEM is also applied to other fields such as biomedical research in creating images of biomolecules with the advantage of high contrast images of samples and allowing imaging of biological samples, without dying samples in advance. Providing high-resolution biology images helps to solve a large number of structural problems in molecular biology. Based on the angular range acquisition of the transmitted electron beam, the imaging modes of STEM can be divided into 3 modes including annular dark field (ADF), high angle annular dark field (HAADF), and bright field (BF). The high spatial images in the DF mode are created using a high-angle ADF detector. The obtained electron signal is the electrons that were scattered away from the direct

beam's path. The atomic number is directly related to the image contrast of an atomic column. In contrast, BF detectors are placed in the transmitted electron beam's path. The BF detectors are positioned in the transmission beam's center to provide images with atomic resolution that show the atomic columns of light elements[43]. For specimen preparation, STEM is not applicable to all materials and structures, it is required to be thin enough for electrons to penetrate the material, so sample preparation specifically is necessity. In addition, it has also been shown from numerous studies that under high-energy, highly concentrated electron beams can cause significant sample damage. The electron beam can be created by several electron sources for instance by Cold-Field-Emission Gun (CFEG) in JEOL JEM-F200 Microscope (Figure 2.3), or the high-brightness field emission gun from the Thermo Scientific Talos F200X STEM.

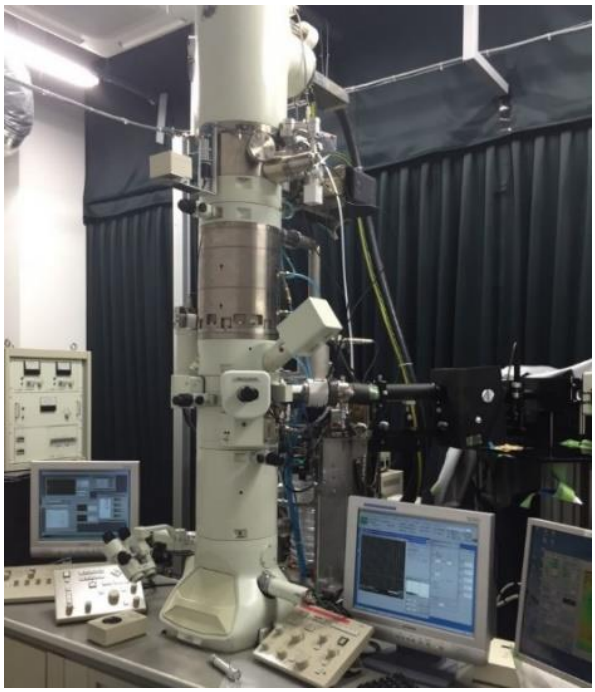

Figure 2.3: a JEOL JEM-F200 STEM

2.5. Cathodoluminescence

CL was first observed when electrons impacted the glass of evacuated discharge tubes, causing light emission. Since then, a whole industry has sprung up in the hunt for superior phosphorescent materials, with CL being widely employed in television displays. CL provides a way for analyzing microstructures while generating the least amount of sample damage. Overall, CL is an excellent approach for studying the optical characteristics of nanostructured materials with nanoscale precision. Other modes of light emission, such as activation of plasmons in metal nanoparticles, exist in addition to e-h pair recombination, which dominates CL in semiconductors. The processes of CL emission are characterized based on their degree of coherence with regard to the external electric field of hitting electrons. Therefore, CL processes can be divided into two categories: coherent and incoherent CL[27][46].

2.5.1. Coherent electron-induced radiation emission

Transition radiation and surface plasmon polaritons are the two primary radiation sources in coherent CL. In contrast, coherent luminescence which is mostly dominant in metals have a correlated phase relation with electron beam excitation. When there is a variation in refractive index in the propagation path of a fast electron, coherent CL is produced. If a substance is in a vacuum, the interface between the material and vacuum allows coherent CL to be generated. When the fast beam excites a substance, it polarizes the material at the electron beam position, resulting in an oscillating charge. Coherent CL corresponds approximately to the radiative EMLDOS at nanoscales, thus, CL can be used to explore the optical properties of materials at the nanoscale[27][26].

2.5.2. Incoherent cathodoluminescence

When the material is activated by an electron beam, the primary electrons decelerate and deposit energy into the substance, resulting in incoherent CL emission. Incoherent radiation such as luminescence generated by electron-hole recombination in semiconductors is usually associated with various types of defects in crystal and

exciton. Incoherent CL is the lack of a fixed phase relation between an emitted photon and an incoming excitation electron, thus does not interfere with coherent radiation[27].

Chapter 3- Short-range ordered plasmonic nanoholes

3.1. Introduction

For SRO nanoholes, each individual hole in the continuous film can generate propagating SPPs through its localized mode, and the interference of SPPs generates the resonance when the SPP wavelength matches the typical inter-hole spacing. This resonance can be employed for surface adsorption sensing since it is sensitive to changes in the environment's dielectric characteristics, which result from changes in the SPP dispersion as well as the local nanohole mode resonance. The refractive index of the SRO nanohole film varies when molecules bond to it, shifting the spectra, which can be accurately detected using a conventional spectrometer[47]. However, the inter-hole distance changes locally as a result of the random arrangement, producing, on average, a broad resonance[2]. Recently, the Anderson localization was effectively seen in a comparable "disordered" nanograting system by modulating the short-range correlated disorder[48]. It was shown that by enhancing the disordering of nanogratings, SPP localization is improved and SPP propagating wave diffusion is prevented. In the metallic nonlinear nanoparticle arrays, Z. Mai et al. have successfully created the Anderson localization[49]. However, to expand the Anderson localized dipole intensity and produce the observed localized mode, a high randomness of the electric driving field is needed. Strong field confinement is produced when several reflected SPPs interfere constructively, according to the Anderson localization of SPPs on a randomly rough metallic surface. Applications that use strong light-matter interactions, optical transition, or random nanolasing benefit from this field confinement and augmentation[50][51][52][53][54]. While such SRO systems are difficult to simulate, crystalline nanoholes are straightforward to simulate by numerical computation. Therefore, an experimental technique is required to study the nanoscopic local field distribution of SRO holes.

In this chapter, we investigate the optical characteristics of SRO and hexagonal crystalline nanoholes on gold-film created by colloidal lithography and a thin film transfer technique employing a self-assembled colloidal mask layer[55]. The optical characteristics of hexagonal and SRO holes are compared to reveal how hole configuration affects plasmon resonances[36][55]. Additionally, it has been noted that the short-range ordered nanohole arrays point to the localized character of the SP, while the periodic hole arrays point to the delocalized nature by considering the magnitude of transmission spectra with different hole numbers[56]. Here, through CL photon maps, we reveal that electromagnetic waves in SRO plasmonic nanoholes are localized by Anderson. When using the CL technique, it is able to visualize EMLDOS, which approximately correlates to the electric field along the beam path at nanoscales[57]. Peak analysis was used to evaluate the spatial distribution of the resonance and strength of the CL spectra at each position. As a result, we experimentally established Anderson localization of electromagnetic waves in SRO nanoholes[53][54][58][59].

3.2. Methods

3.2.1. Nanoholes fabrication

Hexagonal nanohole

Colloid self-assembly was used to create hexagonal nanohole arrays by utilizing PS nanosphere colloids as a mask layer that self-assembled in a hexagonally close-packed arrangement on a flat surface. The creation of a crystalline nanohole array is depicted schematically in Figure 3.1a. We employed a slope self-assembly approach to make hexagonal colloidal masks on a glass substrate. A PS solution with a sphere diameter of 530 nm was employed, with a colloidal solution concentration of 16%. The slope deposition slant angle was fixed at 65^{o}, and the temperature was set at 60^{o}C. The diameter of the PS colloid was decreased during the plasma etching procedure. The thin film layers were then deposited using magnetron sputtering in the order of

aluminum, aluminum nitride, gold, and aluminum nitride. The layer thicknesses are 20 nm, 5 nm, 50 nm, and 5 nm, respectively. For the film transfer, the aluminum layer serves as a sacrificial layer. The colloidal masks were then tape-stripped off. Finally, hydrochloric acid was used to dissolve the aluminum layer, and the floating film on the liquid surface was scooped up with a TEM grid[55].

SRO nanoholes

SRO nanoholes, resembling hexagonal crystalline nanoholes, were fabricated by colloidal lithography and film-transfer on the TEM grid, as in the previous reports[37]. Compared to hexagonal ones, as illustrated in Figure 3.1b, the fabrication method is significantly simpler. Instead of the hexagonal array's crystalline-like arrangement, an amorphous-like SRO colloid layer can be created by drop-coating the colloid solution onto a substrate that has been treated with the aluminum chlorohydrate to create a positively charged surface. The PS colloidal solution (Invitrogen, US, Standard deviation: 8%) contained particles with an average diameter of 100 nm. AlN(10nm)/Au(20nm)/AlN(10) trilayer membrane was deposited using magnetron sputtering after coating the spherical mask layer. After dissolving the aluminum layer, the floating film with the nanoholes was then transferred to a TEM grid.

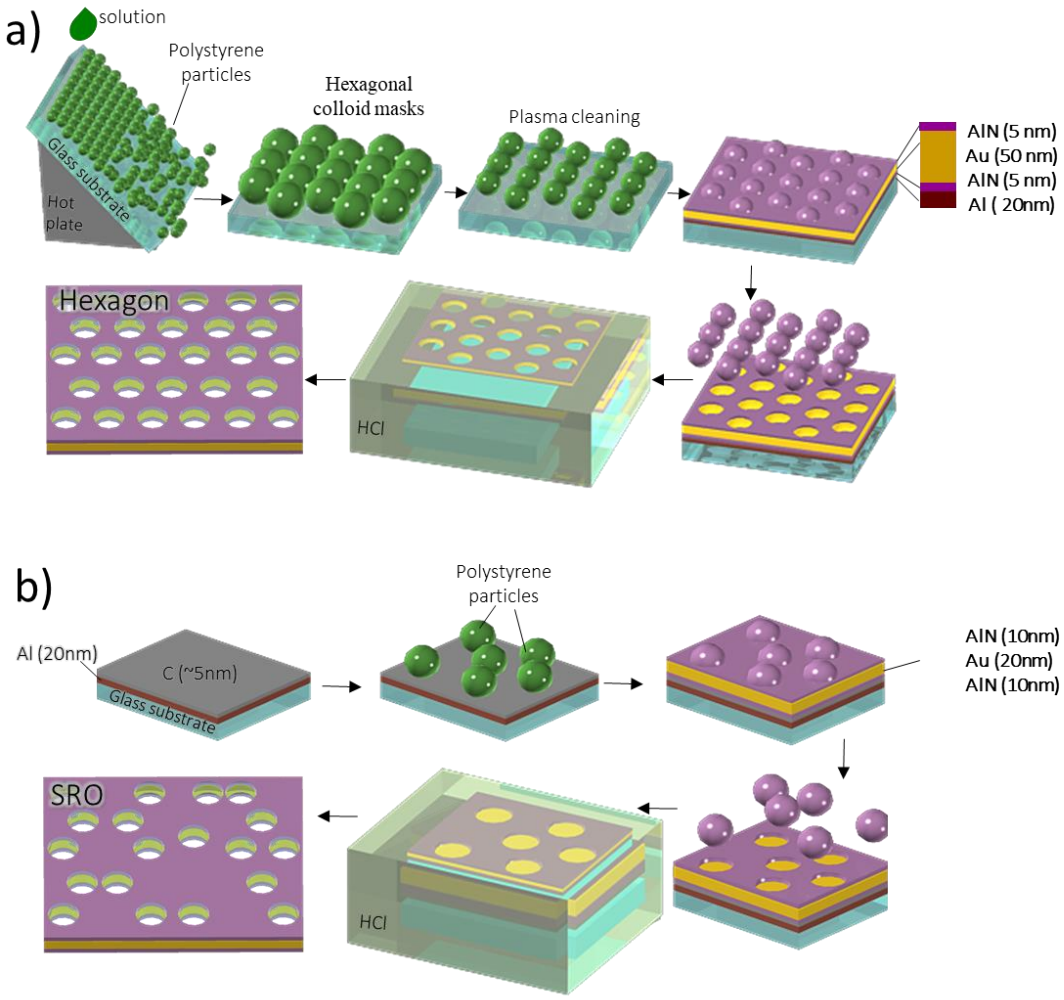

Figure 3.1. Schematics for fabricating hexagonal nanoholes (a) and SRO (b) using colloidal lithography.

3.2.2. FEM simulation

We used COMSOL multiphysics to carry out finite element method (FEM) simulations for the hexagonal array[37]. For gold, literature values for the dispersive refractive index were utilized, whereas aluminum nitride had a constant refractive index of 2.1[60]. The structural parameters were adjusted to match the experiment precisely: 530 nm between hole centers, 50 nm gold layer, and 5 nm AlN sandwich layers. The hole was supposed to have a straight form and a constant diameter from top to bottom. The radiative EMLDOS along the direction of the electron beam correlates to the CL signal[61]. As a result, we positioned the incident plane wave along the surface normal and integrated the square of the electric field of the surface normal component (Ez) above the film surface to simulate the CL spectrum acquired by the surface normal detection. We mapped the field square|Ez|2 30 nm above the surface to compare with the CL mapping[57][46].

3.3. Measurement and analysis

We employ a JEM-2100F STEM equipped with a field emission gun and a CL system, both of which work at an accelerating voltage of 80kV. This technique collimates the light emitted by the specimen by enclosing it in a parabolic mirror. The spectrometer receives the collimated light after that[37][62]. To create a CL photon map, CL signals produced by fast electron optical excitation are acquired at each position of the electron beam as it scans over the specimen[63][64]. A spectrometer with a CCD camera was used to perform spectrum imaging to collect all the CL mapping data (Andor, Shamrock). The radiative EMLDOS's z-component along the beam path is represented by the CL signal[57]. Considering optical reciprocity, the square modulus of the z-electric field $|E_z|^2$ of the existing modes produced by plane wave excitation corresponds to the CL signal[46]. To estimate the CL spectrum more properly, we performed a peak analysis using the CL photon map data from SRO holes. In order to display the position, height, and width of the resonance peak at each electron beam position in the photon map, the peak analysis of the three-dimensional spectral imaging data is carried out. A Gaussian function was used to produce the peak

fitting. Based on the peak analysis, the intensity in the 550 to 800 nm wavelength range is integrated for the panchromatic representation. Additionally, 45 single spectra were extracted from the CL data of SRO nanoholes, and statistical analysis was done to determine the correlation between the hole distance and the position, height, and width of the resonance peak.

3.4. Results and discussion

3.4.1. Hexagonal crystalline nanoholes

AFM and backscattered electron (BE) images of a hexagonal crystalline nanohole sample are shown in Figures 3.2a and 3.2b. The holes' assessed diameter is 320 nm, and the total thickness is around 60 nm. The periodicity inherits the original colloid size. The transmission spectrum obtained experimentally (black line in Figure 3.2c) has Fano-like spectral characteristics with a peak-dip pair near the resonance. This is due to the interference of hole scattering, periodic grating effect, and direct transmission through the film[65]. The transmission spectrum shows a dip at 600 nm and a peak around 750 nm. The integrated CL spectra produced by scanning across a number of holes (red line in Figure 3.2c) exhibits a single peak at 638 nm, which appears between the dip and peak of the transmission spectrum. Because the CL signal is equal to the square root of surface field intensity and there is no interference impact from plane wave illumination, the maximum of the CL spectrum should match to the "real" resonance wavelength. This is also consistent with previous publications explaining the relationship between transmission spectral characteristics and the square of field intensity or absorption maximum[60][65].

Figure 3.2d shows the simulations of the transmission and CL spectra for hexagonal crystalline nanoholes. These results also support the above mentioned explanation. The validity of the simulation model is supported by the agreement between the calculated transmission spectrum's spectral shape and the experimental one. Additionally, the CL signal's excellent agreement with the calculated field strength spectrum ($|E_z|^2$) in this nanohole system is demonstrated by the CL signal's nice match with the experimental CL spectrum. The simulation shows a slight blue-shift in all the spectral characteristics, which can be attributed to the various geometries. Due to the shadowing, which is also evident in the AFM picture in Figure 3.2a, the film surface of the hexagonal hole array created using the colloid mask tends to be non-flat. Due to the angled deposition component and the rise in mask colloid diameter during film deposition, the sidewall of the hole is likewise not straight.

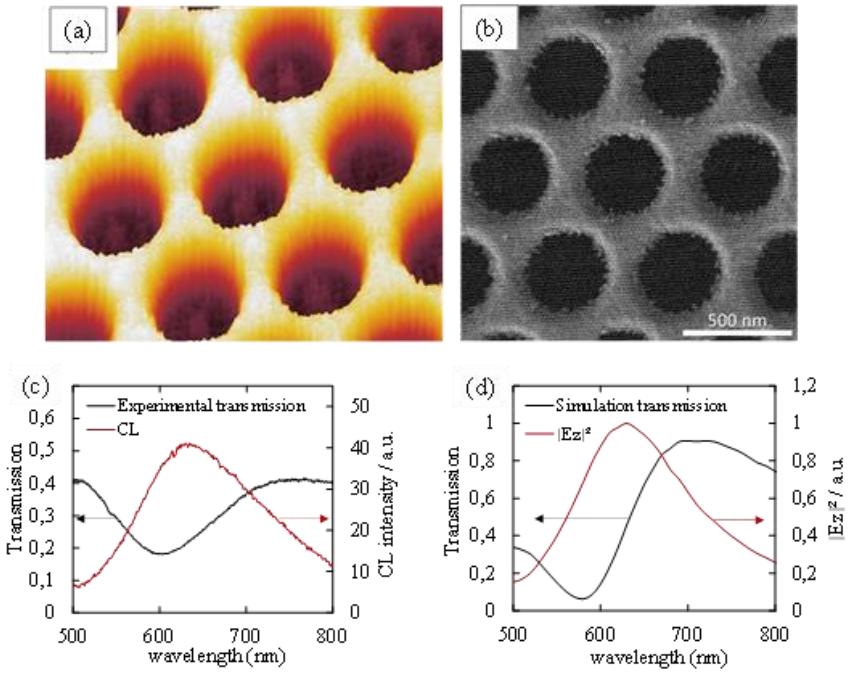

Figure 3.2. (a) AFM and (b) BE images of hexagonal crystalline nanoholes. The hole center-center distance corresponds to 530 nm. (c) The experiment transmission and CL spectra. (d) The simulated transmission and CL spectra of hexagonal crystalline nanoholes.

The hexagonal plasmonic nanoholes at the peak wavelength are presented in Figure 3.3a as a CL photon map (640 nm). In the image, the light emitted from sample was collected in the surface normal direction with polarization in the horizontal direction. According to the photon map, the electric field is localized at the hole edge along the polarization direction, displaying a dipole-like field pattern. In the two-dimensional hexagonal lattice, this pattern reflects the E1 lattice mode[66]. Due to weak emission in the normal direction and wide spectral characteristics, we were unable to observe any further modes.

The experimental CL map is well replicated by the simulated distribution of the square modulus of the electric field along the beam path ($|E_z|^2$) at the resonance (630 nm) in Figure 3.3b. To match the polarization direction of the CL experiment, the incident plane wave was polarized in the image in the horizontal direction. Furthermore, based on the optical reciprocity, this confirms the relationship between the CL signal acquired from the surface normal and the field square modulus $|E_z|^2$[62].

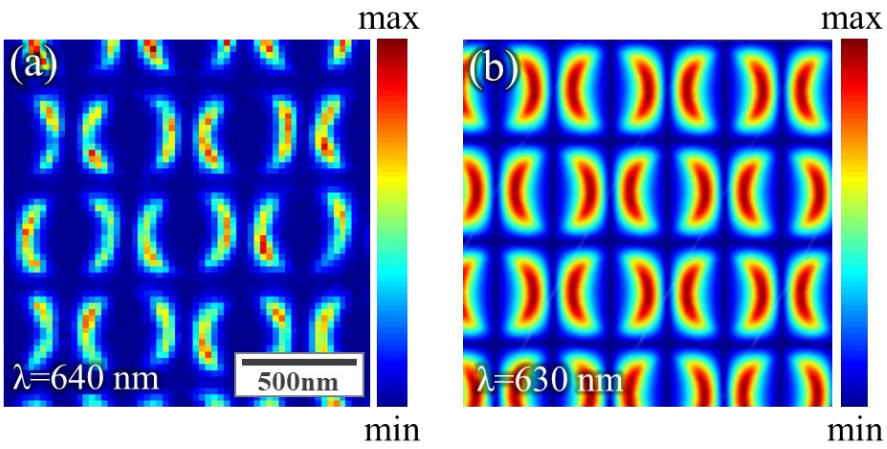

Figure 3.3. (a) A horizontally polarized monochromatic CL photon map of the constructed hexagonal nanohole array at the resonance wavelength (640 nm). (b) FEM simulation of the distribution of the appropriate geometry's z-electric field square $|E_z|^2$ at the resonance wavelength (630nm). 530 nm is the distance from the center of the hole.

3.4.2. Short-range ordered plasmonic nanoholes

Based on the fundamental concepts that the square modulus of the electric field along the beam path in the nanohole system correlates to the CL signal, we here concentrate on the short-range ordered nanoholes that are difficult to simulate. Figure 3.4a presented the STEM bright-field images, of the fabricated SRO nanoholes structured AlN-Au-AlN trilayer, with a diameter of 100 nm. The SRO nanohole arrays are composed of varied distributions of nanoholes. It is possible to control the distribution of SRO nanoholes by changing the concentration of the colloid solution or ionic strength. We fabricated three samples, samples A, B, and C with different hole distributions. The STEM images presented in Figure 3.4a are represented by the corresponding radial distribution functions (RDFs) in Figure 3.4b, where the characteristic peak positions of the RDF curves relate to the typical center-to-center distance between holes. The intensity zero from the RDF curves at fairly close range implies that there is no chance of finding the hole, while its distinctive peak positions represent the typical center-to-center distance between holes. Over 400 nm, the curve approaches one, suggesting that the SRO nanoholes lack of long-range order. In other words, the structure has a disordered azimuthal angle but maintains its typical average hole-to-hole spacing. According to the characteristic distances of the STEM images A, B, and C, which were calculated, they were determined to be around 190 nm, 192 nm, and 208 nm, respectively. The resonance condition of SRO nanoholes may be expressed by this characteristic distance, unlike the resonance condition of hexagonal nanoholes, which is associated to the lattice periodicity.

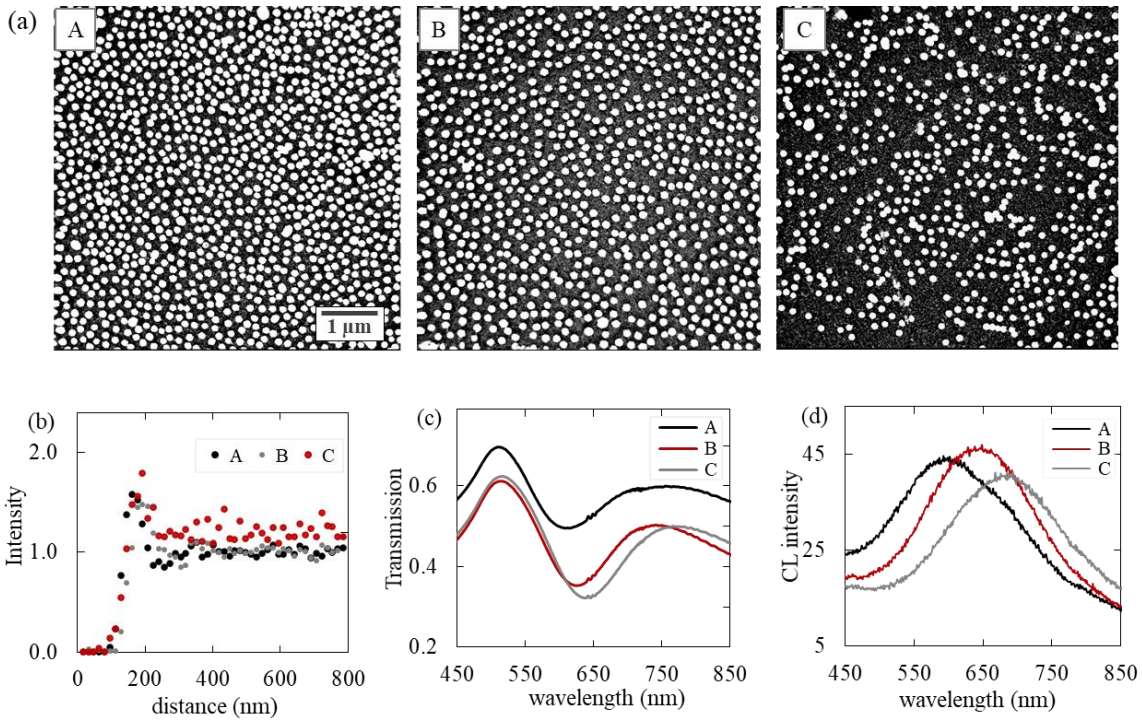

Figure 3.4. (a) STEM images of SRO nanohole sample A, B, and C with different hole distributions. (b) Radial distribution functions calculated for the corresponding STEM images in panel (a). (c) The transmission and (d) CL spectra of samples A (black line), B (red line) and C (gray line).

Figure 3.4c shows the transmission spectra of the samples, all of which include transmission peaks and dips replicating hexagonal hole arrays[67]. Even though all the spectra are similar to each other, distinct spectral shifts and intensity variations are observed. With a characteristic distance of approximately 190 nm and the largest density of holes, sample A exhibits a transmission dip at a wavelength of about 612 nm. In comparison to sample A, samples B and C with lower hole density exhibit significantly weaker transmission intensities and spectral red shift. Samples B and C have characteristic distances of 192 nm and 208 nm, respectively, and their transmission dips change to wavelengths of 620 nm and 644 nm. This red shifting can be explained by an increase in the effective distance in the SPP waves of propagation from the neighboring holes[4][2]. The CL spectra of samples A, B, and C are shown in

Figure 3.4d with the signal integrated across the whole solid angle. The CL spectra show peaks for A, B, and C at 602, 644, and 688 nm, respectively. When compared to transmission spectra, the peak position of CL spectra is all within the range of the transmission dips and peaks. These findings clearly demonstrate that the "true" resonance of SRO holes with maximum field strength similarly occurs between the transmission dip and peak given that the CL signal is correlated to $|E_z|^2$. We believe that this is the first instance in which an SRO system has had its optical resonance examined using both transmission and CL spectra. The difference between the CL peak and transmission dip reveals that the natural resonance of SRO nanoholes should be recognized by field measurements such as CL.

We investigate the local field enhancement in SRO holes with locally variable inter-hole distances since STEM-CL also indicates local field distribution. Figure 3.5a shows a STEM image of the area under investigation, where the holes are dispersed at random and have different inter-hole distances. By step by step scanning the whole surface area indicated in Fig. 3.5a, we can map the CL signal. For certain representative holes that are in a different environment in terms of distance and the number of adjacent holes, we extracted spectra from the collected CL data and plotted them in Fig. 3.5b. The inserted image contains squares marked holes 1, 2, and 3 that highlight the extracted places, with the nearest inter-hole distances are 386 nm, 285 nm, and 171 nm, respectively. When the distance decreases, the peak position in the CL spectrum blue-shifts and broaden.

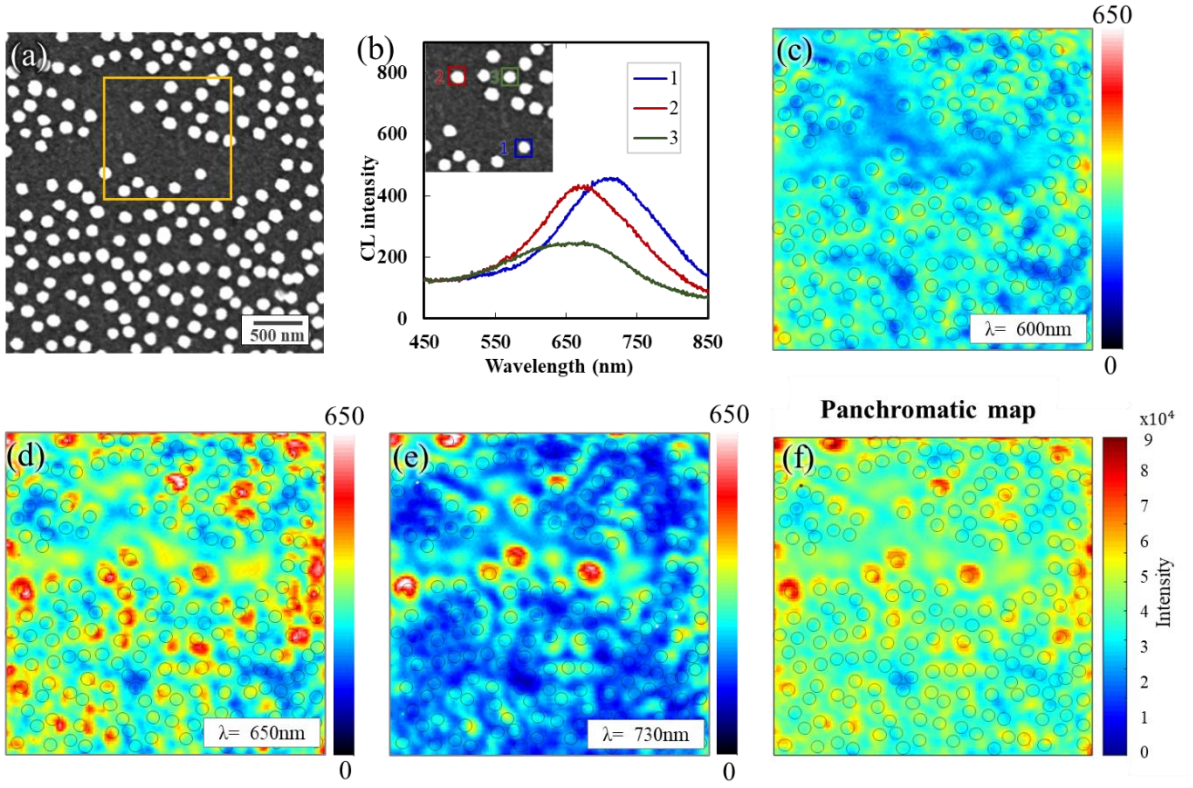

Figure 3.5. (a) STEM image of SRO nanoholes. (b) The extracted CL spectra of holes 1, 2 and 3. (c-e) Monochromatic CL photon maps of the SRO nanoholes at the wavelengths of 600, 650 and 730 nm, respectively. (f) Panchromatic mapping integrated over the wavelength range of 550 nm to 800 nm.

Figures 3.5c–e show CL photon maps without polarization and with complete angle detection, respectively, for wavelengths of (c) = 600 nm, (d) = 650 nm, and (e) = 730 nm. The locations of the holes are identified by the simultaneously acquired STEM bright field image, and the hole edges are indicated by black circles (Fig. 3.5a). The electric field is primarily concentrated at the hole edges for all the selected wavelengths, as can be seen in these CL maps. Even though the size and geometry of each hole are basically the same, the field strength varies at each one. In the CL map at 730 nm, certain holes that are relatively separate from their nearby neighbors strongly confine the electric field at the holes, whereas other groups of holes exhibit basically minimal signal surrounding them. The multiple scattering of SPPs due to their non-periodic configuration and their propagation can account for this inhomogeneity for the

SRO structure[58], [68]–[70]. Even in the large empty regions where there is considerable signal modulation on a flat surface, standing wave-like contrasts are observed at wavelengths of 600 and 650 nm. The remarkable result of the periodicity being disordered is the formation of a complex scattering of SPPs through nanoholes. Multiple subwavelength interferences can be accommodated by the scattered SPPs by the holes, which leads to a strong plasmon localization. This type of field localization of the density of state in disordered systems can also be understood as Anderson localization [53],[56],[58],[62],[63]. In this case, the SRO distribution of the holes causes the EMLDOS, or SPP wave field, to be confined only at specific holes. The panchromatic mapping in Fig. 3.5f integrated over the range of 550-800 nm indicates that the integrated EMLDOS is likewise localized, even if such localization can be found at every wavelength. We notice that for such flat surface systems, the square modulus of the z component of the field accurately describes both the integrated EMLDOS and the charge density[62].

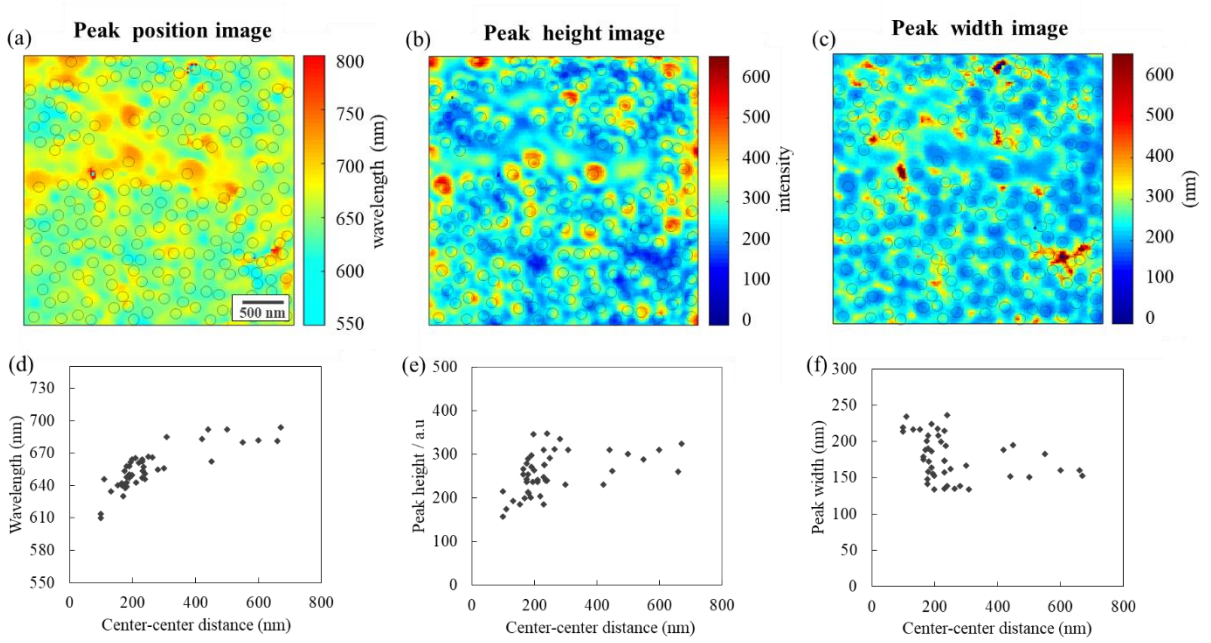

Figure 3.6. Analysis of CL resonant peaks at each mapping pixel. (a) The peak position, (b) peak height, and (c) peak width images of SRO nanoholes are displayed in Fig. 5a. (a-c) post-processed maps using peak fitting. (d-f) Correlation analysis of the SRO nanohole distance versus (d) peak position, (e) peak height, and (f) peak width.

The inter-hole distance is closely related to the strong field confinement, as shown by the wavelength resolved photon maps, however it is not possible to locate the local resonance condition that results from this. We performed peak fitting of the spectrum at each spot of the electron beam in order to extract and characterize local resonances. The peak position, height, and width images of the same region as in Fig. 3.5 can be seen in Fig.3.6. The peak position image shows resonant wavelength ranges between 550 and 800 nm. According to the analysis of the coupled hole resonance described above, it demonstrates that the resonance is red-shifted where the holes are sparsely placed, and the resonance is blue-shifted where the holes are densely packed. The resonant wavelength in the region with no holes is clearly different from that in other dense areas. Similar to plasmonic crystal cavities[71], [72], where the array is locally rearranged to produce various energy levels from the matrix. The corresponding peak height and width images are presented in Figs. 3.6b and 3.6c. Overall, as the inter-hole

distance increases, the peak intensity tends to rise, and the peak width gradually decreases. Figures 3.6d, 3.6e, and 3.6f show the correlation analysis between the fitted values and the hole distance. This clearly indicates that as distance increases, the resonance wavelength redshifts. In Fig. 3.4b's radial distribution function, the characteristic distance is found to be 200 nm, and this is where the plots are accumulated. Although the above- mentioned tendency is correct, the peak height and peak width have a less consistent correlation: as the inter-hole distance increases, the peak height increases and the peak width decreases. The peak height and peak width are unaffected by distance at larger distances than 230 nm. Since the propagation of SPPs determines such resonances at a long distance between the holes, the resonance width is constrained by the long-distance SPP decay length. Additionally, we observe that the ensemble spectrum in Fig. 3.4d are not always as sharp as the local resonance width.

Standing waves mapped in the nanohole membrane through CL maps.The excited SPPs travel along the surface after being irradiated to the electron beam, where they exhibit both reflection and transmission phenomena in the space between the hole edge of neighboring holes. Standing waves may be concentrated on the surface due to the superposition of these waves. At wavelengths of 600 nm and 650 nm, respectively, Figure 3.7 shows a STEM image and the associated CL image. The square-boxed areas in these images include empty spaces that are sufficiently large to make standing wave-like contrasts visible. Because the CL signal relates to the EMLDOS, the high-intensity region correlates to the anti-nodes of the standing waves

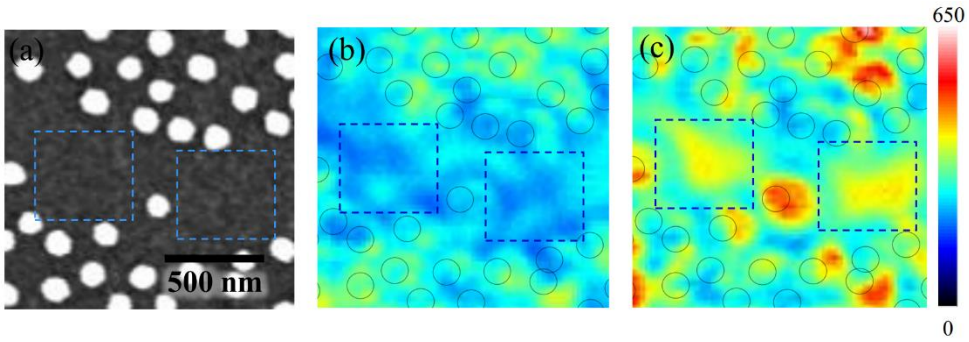

Figure 3.7. (a) STEM image of SRO nanoholes. (b,c) CL photon maps of corresponding to the STEM image area in (a) at the selected wavelengths of (b) 600nm and (b) 650 nm. Square marks indicate the position of standing waves which are confined to the nanohole structure and successfully visualized through the map.

3.5. Conclusion

We have fabricated hexagonal and SRO nanohole arrays using colloidal lithography and film transfer methods. In hexagonal nanoholes, we observed agreement of the experimental CL spectrum and simulated field distribution with the experimental square modulus of the electric field along the beam path $|E_z|^2$. This demonstrated the correspondence of the CL signal detected from the surface normal and the surface normal field ($|E_z|^2$) under the plane wave illumination. The characteristic distance between holes acts as a representation of the resonance frequency of the SRO nanoholes. As the characteristic distance increases, the transmission spectrum dip red-shifts, which is explained by an essentially longer SPP wave propagation length. Likewise to hexagonal nanoholes, the peak position of SRO nanoholes from the CL spectra appears between the dip and peak of its transmission spectra. Unlike the transmission spectrum, which includes interference from the incident plane wave, the peak in the CL spectrum reflects the resonance since the CL signal directly correlates to the field ($|E_z|^2$).

We analyzed local field enhancement in SRO holes, where the inter-hole distance varies locally, through CL photon mapping. The electric field is primarily concentrated at the edges of the holes and is unevenly distributed within holes. The distance between the neighboring holes and the local resonance are correlated. Multiple

subwavelength interferences caused by the SPP's propagation over randomly placed holes leading to Anderson localization of the electromagnetic waves. The insight into the SRO holes obtained here could be applied to the development of broad-band optical devices that incorporate the local resonance over a variety of wavelengths.

Chapter 4 - Luminescence enhancement in MoS_2 flakes through coupling with plasmonic resonance

4.1. Introduction

When single metal nanoparticles are organized in a periodic array, under an appropriate condition of the array period, an additional resonance appear referred as a surface lattice resonance (SLR) due to the scattered field from individual nanoparticles along the plane of the array[7]. A variety of previous studies have been conducted to investigate the optical response of plasmonic nanoparticle arrays since it allows a dramatically sharp resonance, which is outstanding over single nanoparticles[8]. Investigations, for instance, the effect of disorder on the SLRs, the role of lattice symmetry by comparing the SLRs among various period types such as square and hexagonal, or between 1D and 2D lattice[9],[10]. It has always been challenging for such fabricating periodic nanoparticle arrays on large scale since most used technologies such as electron-beam lithography or focused ion beam that are complex and expensive procedures. Therefore, a facile and effective technology, colloidal lithography, can be utilized instead which has been used to easily produce hexagonal periodicity nanoholes using self-assembly of nanospheres. This alternative method, if implemented with an efficient and streamlined process, can achieve a highly ordered array of particles which can be formed over a long range. The easy of fabrication process allows to control the SPR band of particle arrays effectively, to match the excitonic peak of the MoS_2 to eventually maximize optical coupling efficiency[73],[40].

Hybrid structures consisting of the MoS_2 semiconductors and plasmonic nanoparticles have been considered as a great platform for photoluminescent (PL) enhancement due to an exciton-plasmon coupling. For instance, recently the optical response of MoS_2 in the MoS_2-Ag hybrid nanostructures under the illumination by the laser has been studied[23]. As the result, the MoS_2 emission enhanced due to the local fields at the position of the emitters arising from the LSPs of Ag disks. This finding

demonstrated a coupling between the MoS_2 excitons and LSPs in the hybrid structure. PL is commonly used for optical characterization of luminescence materials, however, in CL, the excitation process can be more efficient than PL. CL is excited by a high energy and momentum electron beam. Electrons has a broad range of excitation, while light sources used for PL excitation have a narrow energy range, thus allow probing all transitions from the UV to the IR. CL technique can be used to study nano-photonics and plasmonic materials at very high spatial resolutions that accessibility to very small spatial regions of interest and can provide high resolution information of the electromagnetic local density of states and of the spatial distribution of the excited fields[62]. nanoscale resolution has also been achieved in CL mapping to characterize the near-field local density of states. We believe CL is a powerful approach to explore the emission enhancement of MoS_2 semiconductor in conjunction with plasmonic nanoparticles at nanoscale dimensions. In addition, to our knowledge, plasmonic-exciton coupling and emission enhancement of MoS_2 semiconductor have never been visualized in nanoscale.

In this study, we experimentally visualized a plasmonic-exciton coupling formed in a hybrid structure consisting of MoS_2 flakes on top of periodic Au nanopyramid arrays through CL mapping by means of a STEM-CL technique as described in Figure 1a. Firstly, to maximize the coupling efficiency, it is important to control of the SPR band to match the excitonic peak of the MoS_2 by designing the structure of Au nanopyramid arrays, which is fabricated a combination of colloidal lithography and self-assemble techniques. The radiative electromagnetic local density of state (EMLDOS) in array can be mapped in CL imaging with a nanoscopic resolution which corresponds the electric field distribution along electron beam excitation path[27]. To directly measure energy dispersion of periodic nanopyramid arrays, we employ the four-dimensional (4D) CL technique that allows us to obtain momentum-resolved patterns at excited beam positions, and extract photon energy maps in all radiation angles from the arrays[74].

We then demonstrate a significantly luminescence enhancement resulting from the strongly coupled plasmon–exciton system consisting of Au nanopyramid arrays and MoS_2 flakes. We map the electric field distribution from the hybrid structure and compare it to the field distribution of nanopyramids to determine how the luminescence enhancement is affected by the local field of nanopyramids. By field interaction, approximately 4 times enhanced luminescence of MoS_2 flakes has been observed under an excited electron beam current of 1.13nA. Directly visualizing with a nanoscale resolution, the local luminescence enhancement of MoS_2 flakes due to the plasmonic-exciton coupling, to the best of our knowledge have not been performed yet. Such optical investigation of nanoscale sized excitation sources will be useful for future integrated photonic systems, ultrathin and flexible optoelectronic nanodevices.

4.2. Methods

4.2.1. Fabrication periodic Au pyramids

To fabricate Au pyramid arrays, we use the colloidal lithography technique and self-assembly technique on the water surface using surface tension described step by step in Figure 4.1. Firstly, a glass substrate 1x1 cm is cleaned with DI water and ethanol before plasma cleaning. A scarify layer PMMA with a thickness of 200 nm is spin-coated above 500 rpm for 1minute. After that, a thin carbon layer of about 5~10 nm is deposited above by a thermal evaporator (name of instrument). The purpose of having this layer is to eventually support the Au pyramid array after removing the scarify layer PMMA instead of the glass substrate. After that, we create a mono-hexagonal colloidal mask which is an important step of the colloidal lithography technique to form the periodicity of arrays.

To do this, we make a mono hexagonal PS layer with spheres diameter of 500nm by transferring PS solution to the water surface based on the self-assembly technique of PSs. Firstly, we centrifuge 500ml PS solution under the speed of 300 rpm for 10 minutes to separate water solvent in solution to be floated above and PS nanosphere

layer to be deposited to the bottom. Then, a new PS solution was created by replacing the separated water with a new solvent of ethylene glycol and ethanol ratio 1:2. At room temperature, we transfer the new solution slowly to the water surface and wait for 30 minutes to achieve a homogenous monolayer. After that, the prepared substrate before is used to lift off the monolayer and dry the sample for materials deposition above. After successfully fabricating a hexagonal monolayer mask, we deposited multiple thin layers of AlN/Au/AlN (10/50/20nm) above by using the PVD sputtering method. Follow by that, the mask layer is removed by using tape, then the PMMA is etched with hot water of 90 degrees to finally transfer to a TEM grid by supporting from the bottom carbon layer as shown in the camera image for STEM. The final structure as illustrated, inform a honeycomb period of Au nano-pyramids due to the shadowing effect of the sputtering method (Figure 4.2).

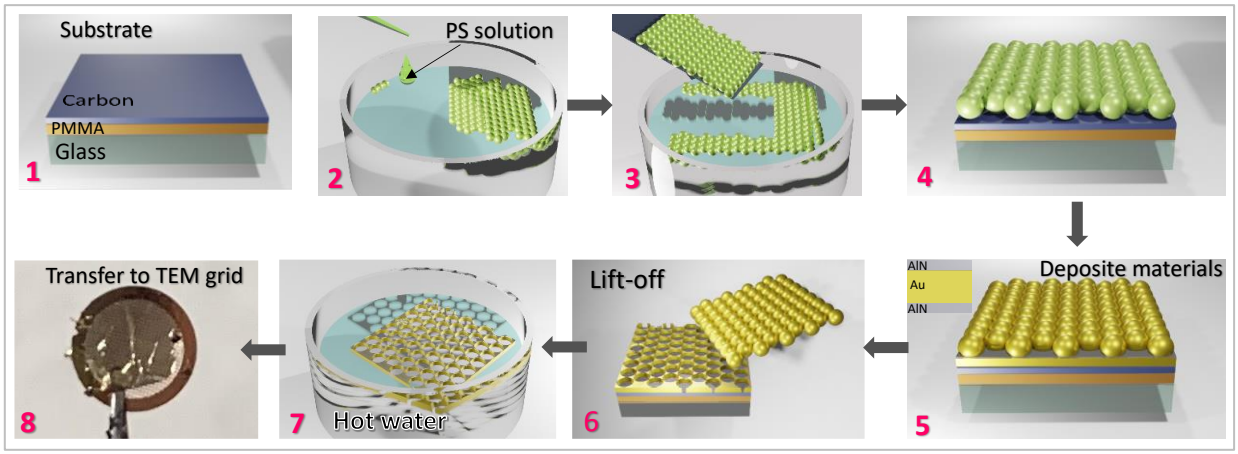

Fig 4.1 Scheme of the fabrication process, using colloidal lithography technique and self-assemble technique of nanospheres on the air-water surface

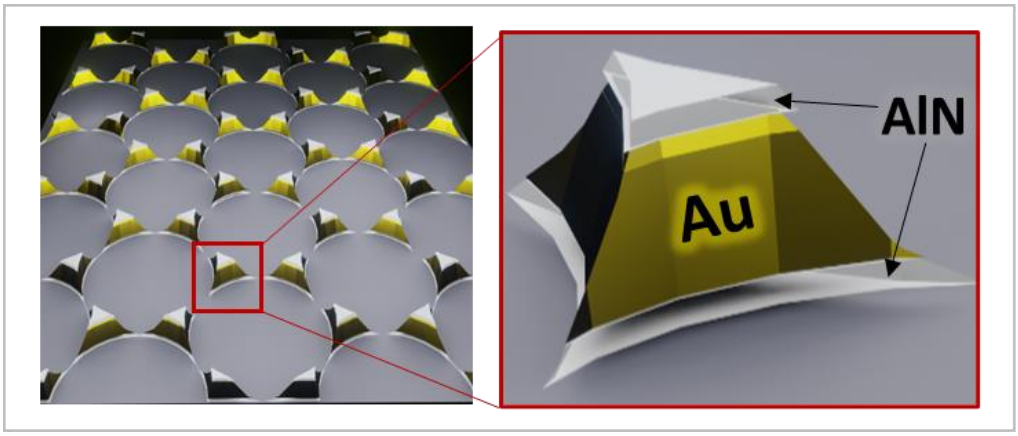

Fig: 4.2 Illustration of the final structure of Au nanopyramid arrays on a flat carbon thin layer.

4.3. Results and discussion

4.3.1. Optical characterization of plasmonic Au nanopyramids

Figure 4.3 shows STEM bright-field and AFM images of both arrays and high magnification images of adjacent pyramid pairs. In general, the array has a honeycomb structure with a period of 433 nm and a total thickness of about 65 nm consisting of three layers of AlN/Au/AlN (10 nm/45 nm/10 nm). The structure of this periodic array is pyramids with the length of the triangular side at the base of 240 nm. Two adjacent single pyramids create an empty space in the middle of about 20 nm. The nanopyramid array is supported by a thin carbon layer of 5~10 nm.

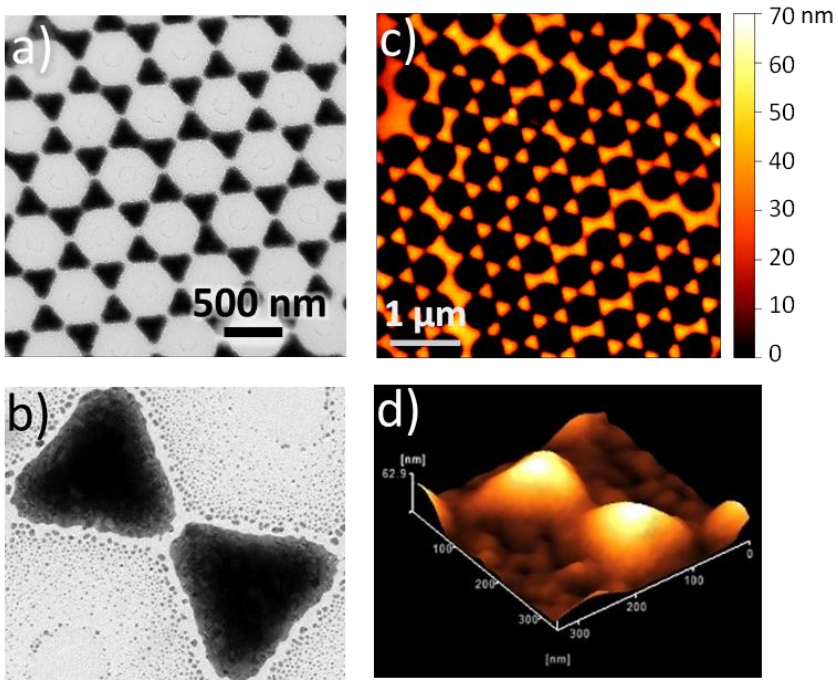

Figure 4.3: Morphology of Au nanopyramid arrays.
(a) and (b) STEM bright-field image of nanopyramid arrays and high magnification image for a pair of adjacent nanopyramids. (c) AFM image of nanopyramid arrays. (d) 3D-AFM image a pair of adjacent nanopyramids.

We investigate the optical properties of pyramidal nanostructures by CL that the signal is collected from all the emission angles without polarization or mask. Figure 4.4a indicates the STEM bright-field image of the measured Au nanopyramids supported on a thin carbon film. CL spectra are measured for three different excitation positions at center of the pyramid and positions on carbon film in the middle of the unit cell. Comparing the spectra of these sites, the spectral intensity is highest at the pyramid with the peak position at about 2 eV. For the remaining positions, the spectral intensity is lower with emission peaks at higher energies. CL mapping shown in figure 4.4 c-e present the field distribution on nanopyramids corresponding to the STEM image in Figure 4.4a obtained at different energies. The dominant energy of this structure is about 2 eV that electric field is relatively uniformly concentrated on the pyramid however it is slightly stronger at the center. For high energies but of lower intensity, the electric field is concentrated on a corner or an edge of the pyramid and is related to the arrangement of the lattice structure. In addition, standing waves occurring on this structure have been captured on the map represented by bright spots and rings observed in maps c and d, respectively. Standing waves such as this are formed from constructive interference enhancement between the diffracted waves from the pyramids propagating in the plane. The energy 2.4 electromagnetic field attributed to the LSPR is provided by single pyramids. This resonance usually depends only on the shape, size, or material the nanopyramid. However, the map shows that its electric field distribution depends on the arrangement of the pyramidal array, suggesting that there is an interaction between the resonant fields.

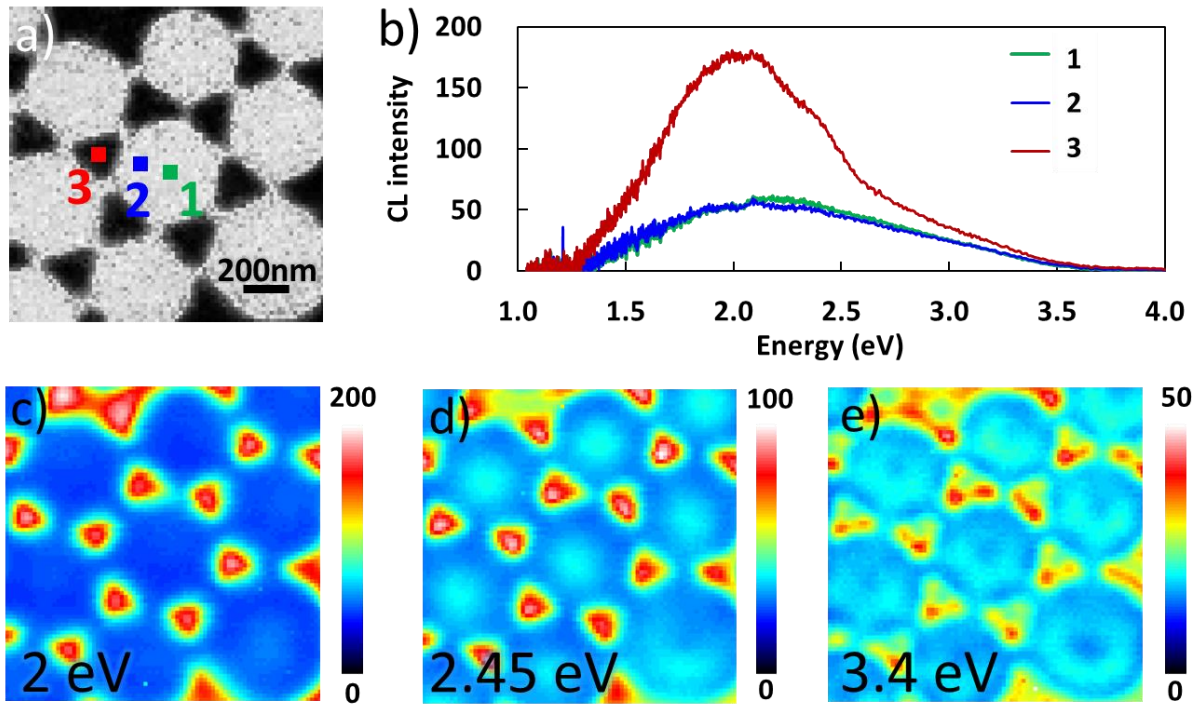

Figure 4.4: Non-polarized CL maps of Au nanopyramids.

(a) STEM bright-field image of Au nanopyramids. CL signals are collected in all the emission angles without polarization. (b) The CL spectra obtained for three excitation positions on the pyramid (in red line), the center of a unit cell (in green line), and the position in the middle between the pyramid and the center of unit cell (in blue line). Here, a unit cell is a circle of 5 pyramids. (c), (d) and (e) CL maps corresponding to the STEM in (a) present field distributions obtained at 2 eV, 2.45 eV and 3.4 eV, respectively. The CL signals were collected from all the emission angles without polarization selectivity.

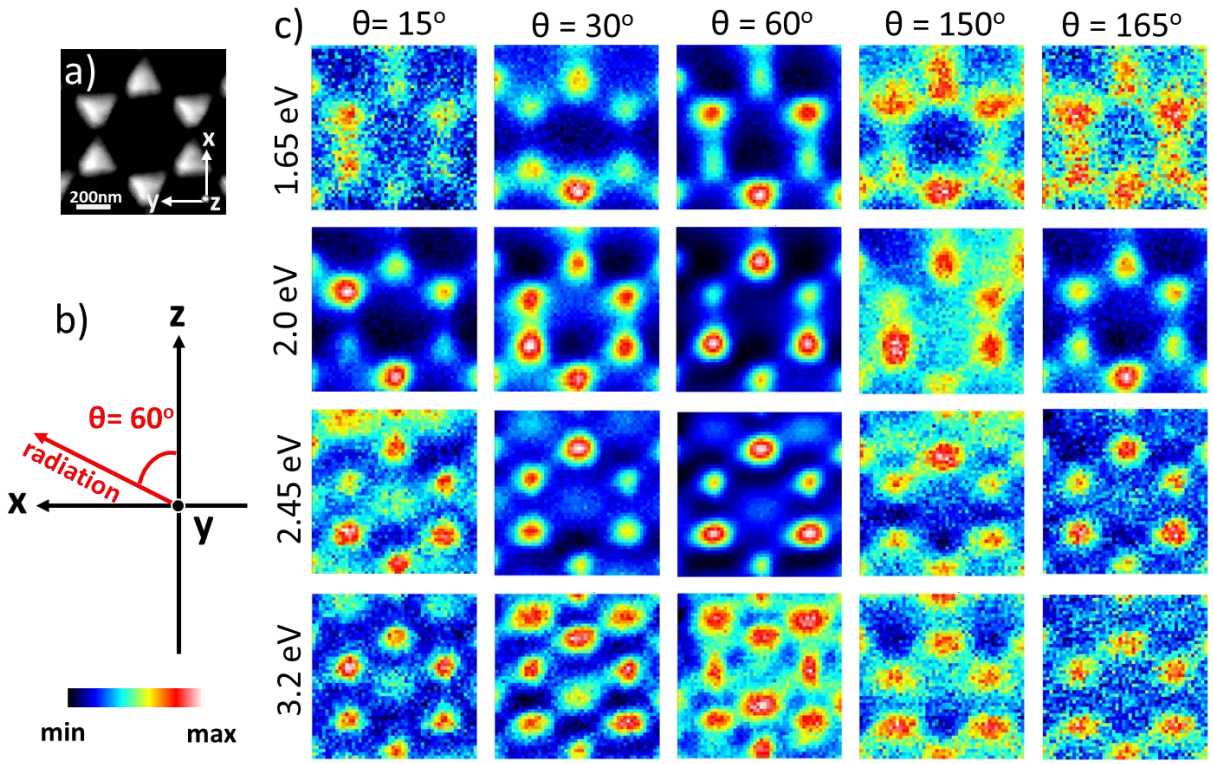

Figure 4.5: P-polarized CL maps for emission modes selected at emission angles.

(a) STEM dark-field image of a unit cell of pyramid arrays (b) Schematic illustration of the detection configuration. The radiated signals obtained at a detection angle ranging from θ = 0–180°. (c) Measured CL maps obtained for p-polarization of the nanopyramids in (a). The maps were obtained for different selection angles θ= 15 °, 30 °, 60 °, 150 °, and 165°

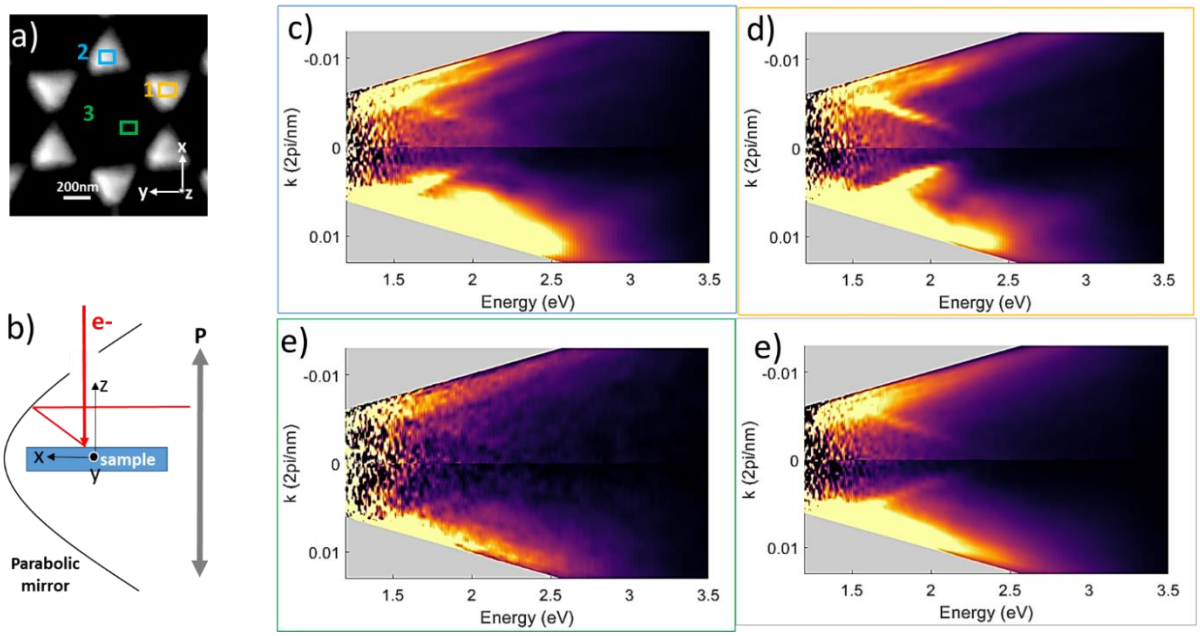

Figure 4.6: a, STEM bright-field image. b, Schematic illustration of the detection configuration. Inserting a slit mask parallel to the z-axis at y= 0 helps obtain the radiated signals at a detection angle ranging from θ=0–180°. (c-e) Photon energy and k vector plots for p polarization.

4.3.2. Luminescence enhancement of MoS_2

Figure 4.7a shows a schematic of the hybrid structure consisting of MoS_2 flakes and Au nanopyramids with a honeycomb arrangement under the electron beam excitation. MoS_2 flakes were drop-casted on the Au nanopyramids supported by a thin carbon layer. The lateral size of MoS_2 flakes in Figures 4.7b and 4.7c are about 800nm and 1.5nm respectively. The contrast of stem and BE images in Figures 4.7b and 4.7c confirms that the hybrid structure consists of the MoS_2 array above the pyramid array. The emission of the entire hybrid structure is represented via a CL map where the signal emission is collected from the entire emission angle. CL map is obtained at 1.9eV which is in between A and B-exciton peaks of MoS_2. From contrast of the CL map, we can compare the emission intensity of MoS_2 flake with and without exposure to the underlying nanopyramids. Firstly, it can be seen on the CL map that due to the periodic structure of the pyramid array, we can determine their positions, which are bright spots of moderate intensity and uniformity. Although the MoS_2 flakes has a flat surface as confirmed by the BEI image, its emission intensity shown on the CL map is not uniform across the entire scale. In MoS_2 flake areas, there are spots with a higher intensity whose positions are confirmed to be MoS_2/nanopyramids by comparing with the stem image and based on the periodicity of the pyramid array. We then extract the CL spectra of MoS_2/au pyramid along with the MoS_2 and Au pyramids shown in Figures 4.7b and 4.7c their positions indicated on the stem by square markers. It shows that the peak intensity at MoS_2/au is approximately 3 times higher than that of MoS_2 or the au pyramid. We also compared the peak intensity of MoS_2/au with the sum of two separate spectra MoS_2 and pyramid au to further investigate whether the increase in emission intensity at MoS_2 is due to an enhanced interaction with au pyramids or simply a spectral overlap of au pyramids and MoS_2. As a result, the intensity of MoS_2 is 1.5 times higher than sum of Au and MoS_2, revealing that there is an optical interaction that enhanced the MoS_2 exciton emission. This enhancement is the result of a coupling between plasmonic field from au pyramids and exciton dipoles in MoS_2.

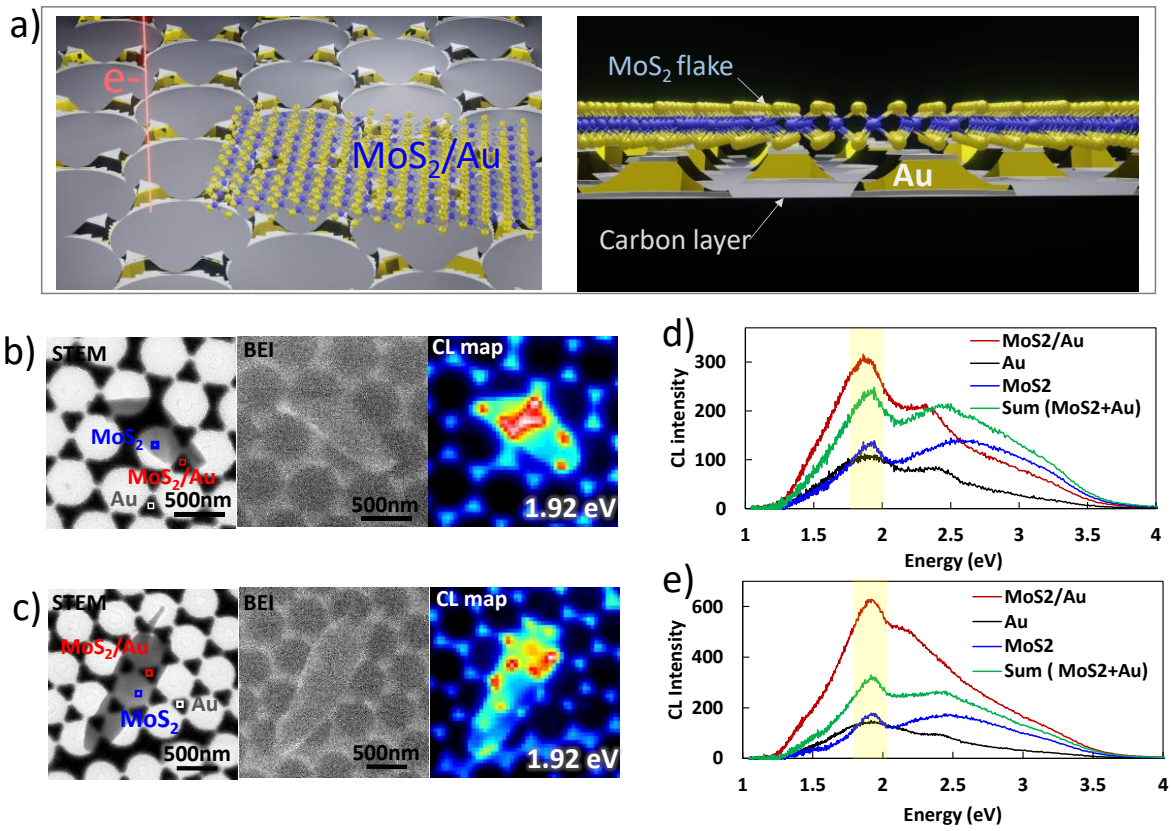

Figure 4.7. Structure and CL properties of MoS_2-Au pyramids hybrid structure. a) Schematics of MoS_2-Au pyramids hybrid structure, where MoS_2 flakes were drop-casted above the Au nanopyramid arrays which supported by a thin carbon layer. b) and c) STEM bright-field images, BE images and corresponding CL maps of two positions of MoS_2-Au pyramids hybrid structure. d) and e) CL spectra extracted from CL maps in b and c for MoS_2 (in blue line), Au pyramids (in black line), MoS_2- Au pyramids, and sum of MoS_2 plus Au pyramids (in green line). CL signals were collected normally from all radiation angles without polarization and masks.

It is also observed that the enhanced emission intensity is unequal between the MoS_2/Au locations within a single MoS_2 flake. The extracted spectra for MoS_2/Au locations of samples are presented in Figure 4.8. This can be explained by the uneven contact distance between MoS_2 and the pyramid or because the height of the pyramid is not completely equal as can be seen from the contrast of the AFM image on the Figure. 4.3.

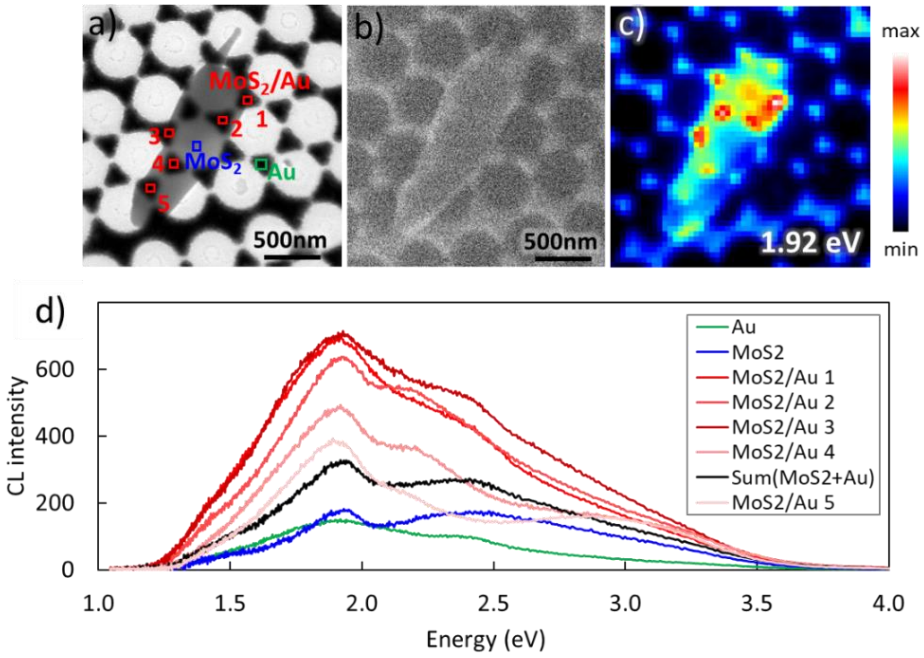

Figure 4.8: a, STEM bright-field images. b, BE images and c, corresponding CL maps of MoS_2-Au pyramids hybrid structure. d, CL spectra extracted from CL maps c for MoS_2 (in blue line), Au pyramids (in black line), MoS_2- Au pyramids, and sum of MoS_2 plus Au pyramids (in green line). CL signals were collected normally from all radiation angles without polarization and masks

In addition, an important reason for this result is that the thickness of the MoS_2 flake is not uniform leading to uneven emission enhancement within the same flake. To clarify this, we investigate the enhancement of a different MoS_2 flake with the thickness difference observed more clearly in Figure 4.9 based on the contrast of the STEM and BE images. From the map and individual spectra extracted from the CL map data, the results show that, when interacting with pyramids with the same field strength, within a MoS_2 flake, the locally enhanced emission intensity is stronger at the

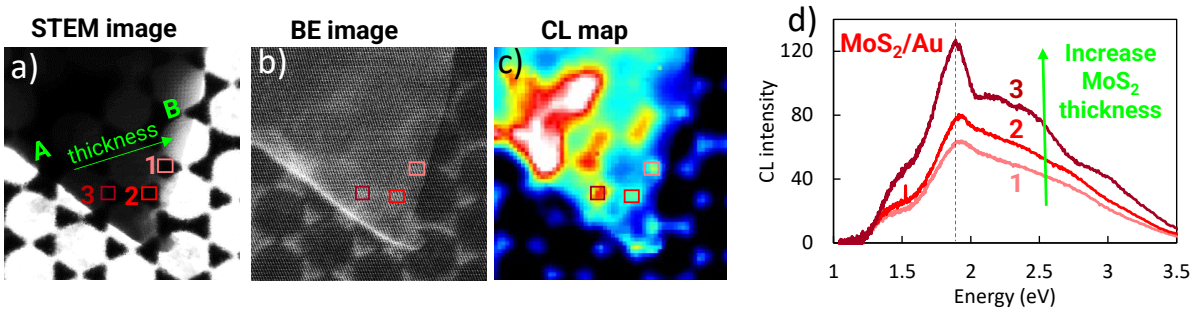

position where MoS_2 flake is thicker.

Figure 4.9: STEM bright-field images. b, BE images and c, corresponding CL maps of MoS_2-Au pyramids hybrid structure. From A to B, the thickness of MoS_2 flakes decrease. d, CL spectra extracted from CL maps c for MoS_2- Au pyramids 1, 2 and 3 marked on a with decreasing thickness. CL signals were collected normally from all radiation angles without polarization and masks

Finally, the dependence of the emission enhancement of MoS2 on the excitation current is realized. Because the hybrid structure in this study includes both incoherent and coherent CL, we wanted to examine whether the response of mos2, of Au and of mos2/Au is different when bombarded with the beam at different electron speeds. Figure 4.10 shows that the emission distribution on the map is different when the electric field change is especially pronounced at emission energy 2.3eV. The integrated spectrum also shows that the ratio of emission peaks in the spectrum changes significantly. At 1.13nA the exciton emission peak intensity is sharpest, then becomes wider when the current is 23 nA. This may be due to the saturation of MoS2 exciton emission for the high current, while the plasmonic intensity from Au increases linearly with the magnitude of the current. However, it is also possible that there is damage to the sample caused by the electric field, thus, the evaluation of the self-dependence of the emission on the current becomes more complicated in practice.

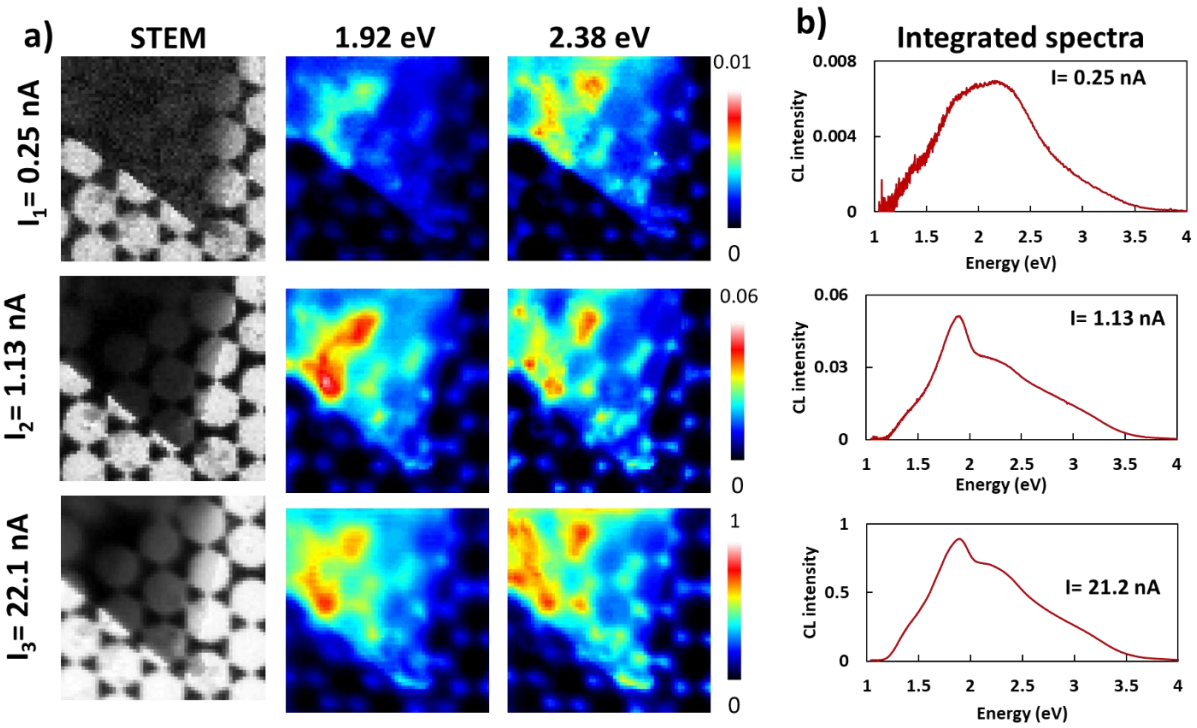

Figure 4.10: Electron beam current dependence. MoS_2/ Au pyramids is measured with different currents. Electron beam current increase from the top to the bottom. a, STEM image and CL maps. b, integrated spectral from the CL map in a.

4.4. Conclusion

In this chapter, we presented the first method to enhance the luminescence of MoS_2 using a plasmonic Au nanopyramid structure. The periodic Au nanopyramid array is fabricated using colloidal lithography and film transfer techniques. Optical characterization of plasmonic Au nanopyramids is investigated through CL measurement, including field distributions and information about emission angles for certain energies. Generally, the plasmonic resonance of nanopyramids was measured to be around 2 eV which overlaps the A- and B-exciton emissions of MoS_2. Then, the hybrid structure is fabricated consisting of MoS_2 flakes and periodic nanopyramids supported by a thin carbon layer in the bottom for the optical interaction enhancement. Through high-resolution CL maps, we have successfully visualized local luminescence enhancement in MoS_2 flake, due to the coupling with the local electric field supported by Au nanopyramids underneath. In addition, we observed the enhancement intensity depends on the thickness of MoS_2 flakes. When interacting with pyramids with the same field strength, the locally enhanced emission intensity is stronger at the position where the MoS_2 flake is thicker.

Chapter 5- Exciton-dielectric mode coupling in MoS_2 nanoflakes

5.1. Introduction

Materials belonging to the TMDC family can have high refractive indices in addition to exciton emissions[14]–[19] and can confine an optical field to improve the interactions between light and matter by creating dielectric cavity modes[20], [21]. It has been established that WS_2 nanodisks made of multilayer WS_2 have qualities that allow for the coupling of Mie resonant modes induced in nanostructures sensitive to geometrical parameters and A-excitons arising from the intrinsic material properties of WS_2[14]. In this chapter, dielectric resonant modes that produce light in the visible spectrum, and its coupling with intrinsic luminescence. Visualization of the optical properties beyond the diffraction limit of light is necessary to probe and comprehend the origin of the sub-wavelength optical properties of the MoS_2 nanostructures, particularly for the identification of the unique mechanisms underlying the various types of light emission[26], [27]. This is achieved by utilizing an electron beam as a high-energy and high-momentum excitation source with a size of down to 1 nm, resulting in the excitation of all electron transitions in the material with nanoscale precision, which photoluminescence spectroscopy does not allow[30],[91],[92]. However, there is currently no nanoscopic measurement accessible in the literature that investigates the optical response of TMDCs at nanoscale scales.

CL has been used to investigate the composition and defects of material structures, and it is also commonly employed to investigate the influence of dopants in insulators and semiconductors, as well as to investigate optical modes in nanophotonics[77],[78]. As a result, we believe that CL is an effective method for obtaining the nanoscopic optical information of MoS_2. In this chapter, we use a CL-STEM system to experimentally visualize emission processes supported in single MoS_2 nanoflakes. We begin by mapping the photon emission distribution on individual nanoflakes and comparing emission wavelengths for different flake geometries. The resulting CL

mapping data is then spectrally deconvoluted in order to separate the overlapping emission modes of nanoflakes, and the dielectric mode is recognized additionally based on the field distribution. We explore how the resonant modes contribute to luminescence enhancement based on the observed deconvoluted peaks. Furthermore, because measured CL signals are superpositions of several emission modes, we use the four-dimensional (4D) CL method[74] that enables us to extract photon energy maps from the flake in all radiation angles and get the angular spectrum at stimulated electron beam position.

5.2. Methods

5.2.1. CL measurement

Similar with chapter 3 and chapter 4, in this chapter we use the CL system which is a combination of a JEM-2100F STEM (JEOL Ltd.) performed at 80 kV electron acceleration voltage and an optical detection system with a 1 nm spatial resolution [62],[46]. For the 4D CL system[74], Behind the objective lens, polarizers, and masks, a slit mask is inserted in the radiation channel parallel to the z-axis. The radiation is transmitted to the spectrometer through the optical system, with information on the emission angle dependency projected along the vertical axis. Therefore, 4D STEM-CL simultaneously obtains the angular distribution and spectrum at each beam position. To produce a CL photon map, the CL signals emitted by optical excitation by fast electrons are captured at each electron beam point as the electron beam scans over the material. However, the broad overlapping peaks in the raw spectra from the CL photon map data had proved difficult to identify. We used Lorentzian fitting to do spectrum deconvolution on the CL photon map data, allowing us to provide the deconvoluted CL mapping to reveal the original energy modes in the MoS_2 flakes. By depositing the MoS_2 flake solution onto an elastic carbon grid, the TEM specimen was prepared (Okenshoji Co., Ltd., Japan).

5.2.2. BEM Simulation

We perform BEM simulations within the MNPBEM toolbox to reproduce CL emitted by MoS_2 nanoflakes[79]–[81]. BEM simulations are based on calculating spectra with Maxwell's equations. To be compatible with CL measurement conditions, the simulation CL signal is generated by an electron beam with an electron acceleration voltage of 80 kV. The simulation also allows the CL radiation signals to be resolved in terms of polarization and detection angle by angularly rotating the detector around the structure.

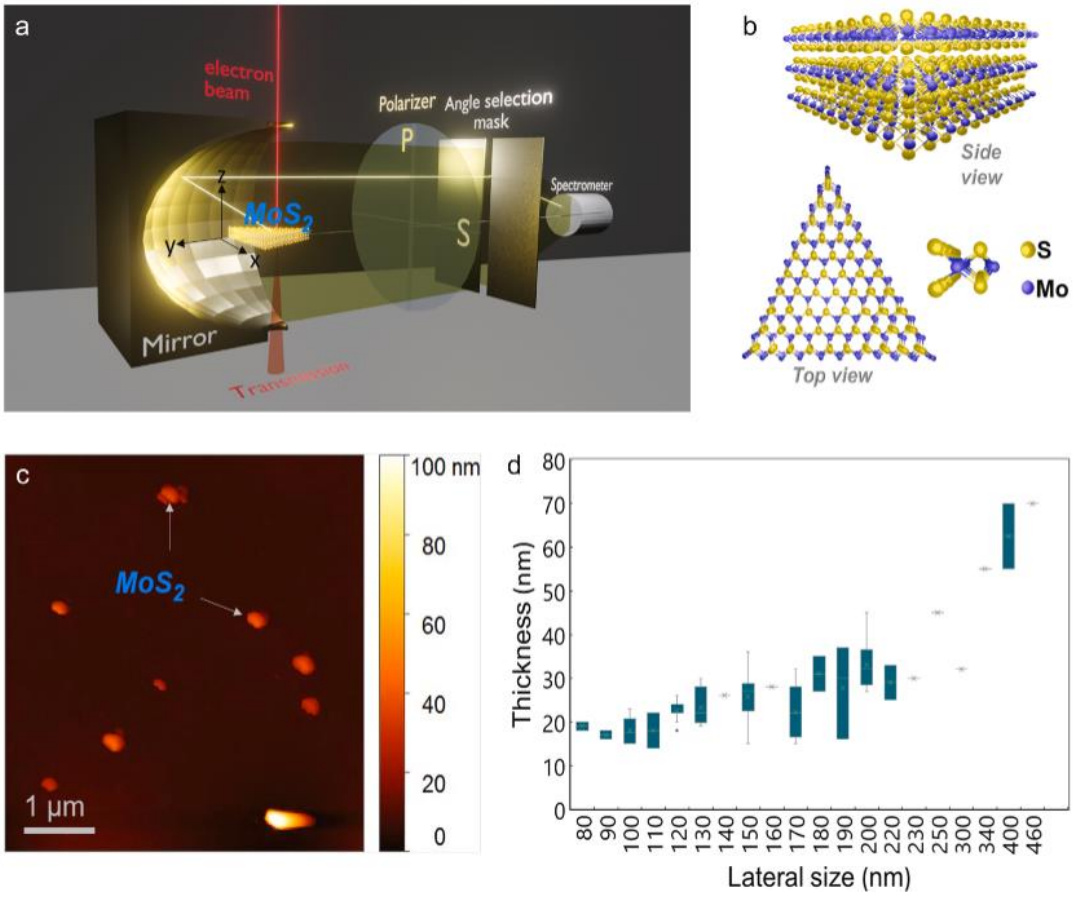

Fig. 5.1: CL-STEM experimental setup and sample morphology (a) STEM-CL system schematic. (b) A triangular multiple-layer MoS_2 crystal structure. Molybdenum atoms (blue) are sandwiched between two layers of sulfur atoms in monolayer MoS_2 (yellow). (c) The AFM picture of MoS_2 flakes on a flat substrate. (d) AFM measurements of the lateral size and thickness of flakes

5.3. Results and discussion

5.3.1. Emission modes of isolated MoS_2 nanoflakes

We identify the optical modes of the MoS_2 in this section by collecting radiated emission from the whole range of emission angles provided by the parabolic mirror (Figure 5.1a). Figure 5.1b illustrates the crystal structure of a triangular flake, which is responsible for the typical flat and thin structure of small flake. Figure 5.1c shows the AFM images of the used MoS_2 flakes (Nanoflake solution, EM-Japan Co. Ltd., Japan) on a flat substrate. Figure 5.1d describes the relation between thickness and lateral dimension acquired from AFM images of several flakes. According to Figure 5.1d, Figure 5.2a exhibits a bright-field STEM image of a triangular MoS_2 flake with a lateral size of 160 nm and a thickness of approximately 30 nm. Line-scan spectra obtained by positioning the electron beam at positions 1-3 of the flake as labeled in Figure 5.2a are shown in Figure 5.2b. The spectra are significantly dependent on the excitation position, with position 1 having a larger CL intensity than positions 2 and 3. The CL spectra of the nanoflake consist of many overlapping energy peaks, thus they are fitted with a multiple to better explain this phenomenon. To further understand this phenomenon, the CL spectra of the nanoflake are fitted using a multiple peak model that reflects the optical modes of MoS_2 that are currently known. The CL spectra of the nanoflake consist of many overlapping energy peaks. The multiple peak fitting for the spectra obtained at the 1 and 2 locations, respectively, is shown in Figures 5.2c and 5.2d. In this, the A-exciton and the B-exciton, which occur owing to a direct and an indirect bandgap, respectively, are attributed to the A peak at 1.84 eV and the B peak at 2.03 eV[15], [82], [83]. The C peak at 2.78 eV corresponds to the C-exciton, which results from transitions between the highest valence band and the first three lowest conduction bands of MoS_2[84],[85]. As reported by V.L. Le[86], the exciton transition band at the M point of the MoS_2 band structure is responsible for the E_1 peak at 3.15 eV. We also see a significant peak at 2.5eV (E_d) that does not correspond to any known MoS_2 exciton transitions and is strongly dependent on excitation position. As will be

detailed later, the energy of the Ed peak varies with the shape and size of the flake, therefore E_d may be attributed to a geometrically dependent dielectric resonant mode induced the high refractive index of MoS_2[14]. If the flake form enables non-degenerate dielectric modes, one structure can support several dielectric modes. In addition, despite the relatively uniform thickness of the flake, the exciton peaks A and B increase greater for edge excitation rather than center excitation, implying the existence of a luminescence enhancement mechanism at the edges.

Figure 5.3 shows non-deconvoluted and deconvoluted CL maps selected at mode energies corresponding to the same flake as in Figure 5.2a. The intensity of each emission peak is presented separately in deconvoluted CL maps, excluding overlapping spectra from neighboring peaks. The deconvoluted field distribution seems to be uniform across the whole surface at the maximum energy peak of 3.15 eV (E_1 exciton), however it is most strongly concentrated to the corner of flake at 2.45 eV. Unlike the E_1 exciton, the field is more strongly focused at the edges of the flake at 2.78 eV while maintaining a reduced but uniform emission throughout the entire flake surface. By contributing to the amplification of the exciton-related luminescence at energy levels overlapping or below the E_d peak, the E_d resonant mode can increase the efficiency of the production of electron-hole pairs. When the exciton states are electromagnetically coupled with the E_d resonant mode, radiative recombination can also be enhanced via the Purcell effect in addition to this excitation enhancement. The deconvoluted CL maps clearly show that the presence of the E_d resonant mode causes either the excitation or Purcell enhancement (or both) to improve the luminescence efficiency of the A and B excitons at the corners[87],[88]. Because the dielectric resonance peak is broad, the coupling is insufficient to produce a peak split[89],[90]. According to the spectral deconvolution mapping, the E_1 mode at energy 3.15 eV is not connected to the dielectric dipole mode for this flake, unlike the remaining A and B modes that may be coupled to the dielectric dipole mode. While exciton emissions from multilayer MoS_2 flakes have been observed in photoluminescence (PL) measurements[11], such local emission enhancement can only be achieved using high

spatial resolution measurements such as STEM-CL. It should also be noted that, unlike

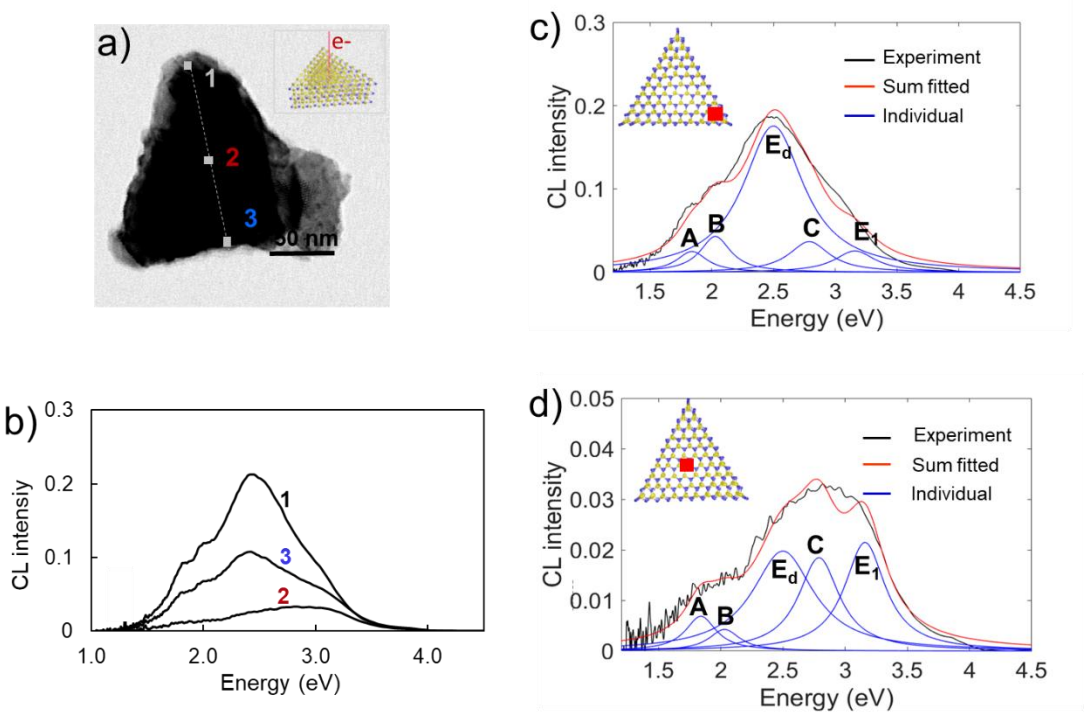

conventional PL, CL comprises both incoherent and coherent emissions.[27],[89],[90].

Fig. 5.2: (a) STEM bright field image of a single triangular MoS_2 particle. The inset illustrates an electron beam impinging on a triangular MoS_2 nanoflake. Figure 2a shows line-scan CL spectra along electron beam locations 1 to 3. (c) and (d) The spectra obtained for stimulation at the flake edge and core, respectively. Fitting the experimental data (black line) to a sum of separate Lorentzian curves is used to conduct spectral deconvolution (blue lines). Individual curve peaks are 1.84 eV (A-exciton), 2.03 eV (B-exciton), 2.45 eV (Ed), 2.78 eV (C-exciton), and 3.15 eV. (E1).

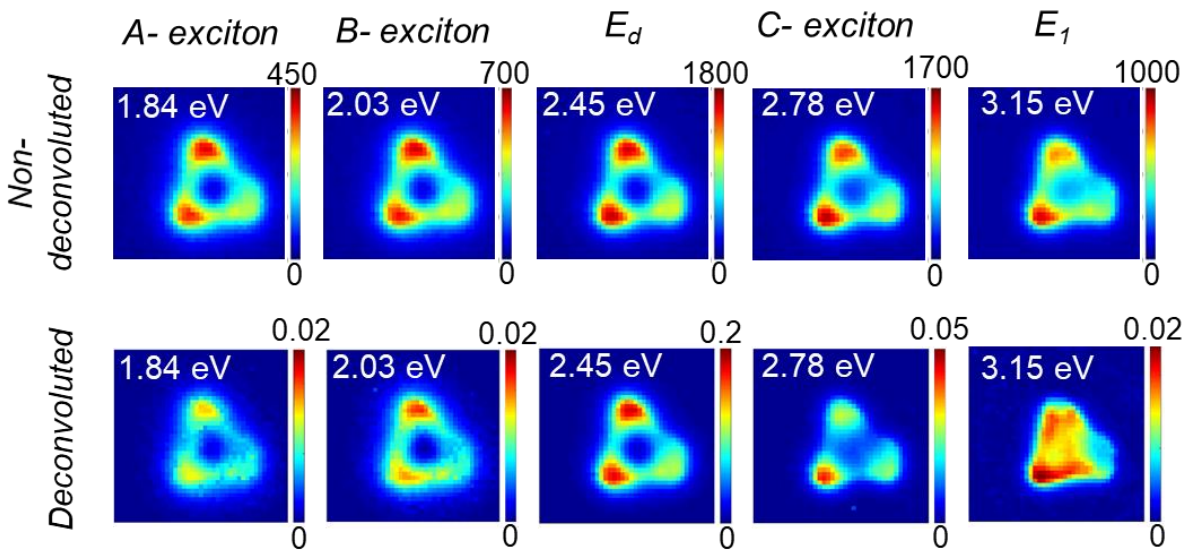

Fig. 5.3: Non-polarized CL maps with and without spectra deconvolution at 1.84 eV (A-exciton), 2.03 eV (B-exciton), 2.45 eV (Ed), 2.78 eV (C-exciton), and 3.15 eV (E1), as illustrated in Figures 5.2c and 5.2d. Mapping data is obtained from the same flake seen in Figure 5.2a. CL signals are captured from all emission angles without polarization selectivity.

5.3.2. Shape dependence of emission modes

We also investigate how different flake shapes affect dielectric resonance modes. STEM bright field and BE images in figure 5.4 support the morphologies of the investigated flakes. An oval (Figure 5.4a), rectangular (Figures 5.4b and 5.4c), and triangular-shaped flake (Figure 5.4d) with lateral diameters between 150 and 250 nm are shown in the figure from top to bottom. By collecting the transmitted signal from all directions, CL maps that correlate to the flakes are created. The fixed energies of A, B, and C exciton modes and the variable energies of dielectric resonance modes, which depend on the flake dimensions, are both fitted to deconvoluted CL maps. The figure 5.8 also discusses how the mode is affected by flake size. The edges or corners of the flakes frequently show hotspots in these resonance modes. Some shapes support more than one dielectric mode while others only one. For instance, in the CL maps of the rectangular flake in figure 5.4b, hotspots at the structure's long axis edges correspond to a low energy mode (E_d of 2.4 eV), whereas hotspots at the structure's short axis edges correspond to a higher energy mode (E_d of 2.73 eV). The energy difference

between the two modes results from the structure's length and width. The field hotspots are situated at the corners of the smaller triangular flake, which has almost identical edge lengths, but only supports one resonance mode energy E_d at 2.67 eV. It is observed that CL maps for the A, B, and E_1 emission patterns are affected by the dielectric modes, further supporting the theory that the exciton emission is coupled

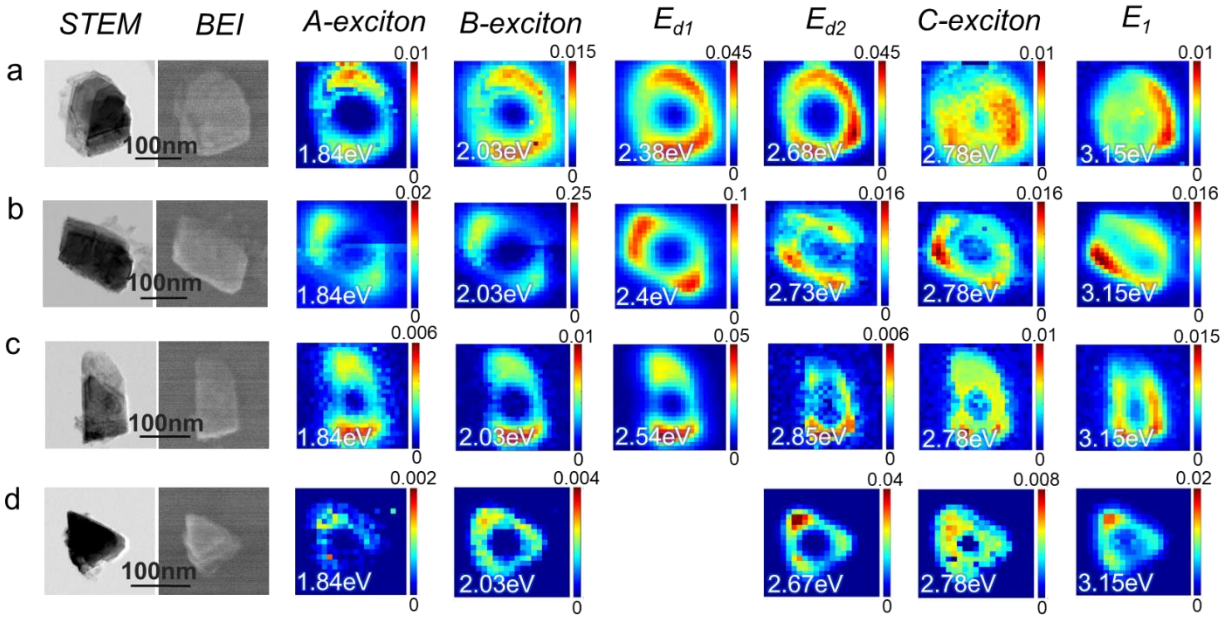

through the excitation of the dielectric mode.

Fig. 5.4: Non-polarized CL maps of individual MoS_2 nanoflakes with different shapes and sizes. STEM bright field and BEI images, and deconvoluted CL maps experimentally observed for different shapes: (a) oval, (b), (c) rectangular, and (d) triangular nanoflakes respectively.

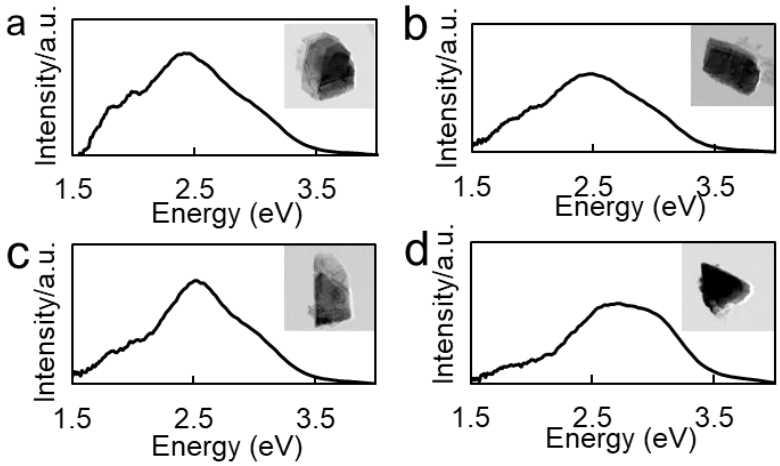

Fig. 5.5: The experimental CL spectra for the corresponding flakes indicated on figure... CL signals are collected in all the emission angles without polarization.

5.3.3. Comparison of experiment and simulation with polarization

We now conduct a more thorough mode analysis using numerical simulation and polarization-dependent CL mapping. To illustrate how the modes are polarization dependent, a rectangular flake was chosen as a model. The radiative electric field with p- and s-polarizations for the rectangular flake illustrated in Figure 5.5 is visualized in order to study the polarization dependency. The STEM image and BE images of the measured rectangular MoS2 flake are shown in Figure 5.5a. The CL system is set up in Figure 5.5b with the s-polarizer perpendicular to the x-z plane and the p-polarizer parallel to it. The identical flake from Figure 5.4c was measured using the s- and p-polarizations seen in Figure 5.5c.

The experimental data is compared with simulation by BEM[80], [91], [92] for a rectangular MoS_2 flake with a width of 100 nm, a length of 200 nm, and a thickness of 28 nm, which approximately corresponds to the size of the measured flake. Figure 5.8 includes the measurement and simulated spectra that were obtained from this rectangular flake. The distributions of the generated hotspots correlate well with the experimental and simulated CL maps in Figures 5.5c and d. High energy hotspots are situated along the short axis while lesser energy hotspots are positioned along the long axis in the non-polarized maps where the emission from all angles is gathered. We separately plot the p- and s-polarized maps in order to better comprehend this. The hotspots are distributed along the long axis in the p-polarized simulation maps for all energy, with smaller energies having larger relative intensities[93]. This finding demonstrates that the coherent excitons' dipolar momenta are parallel to the long or short axes[94],[95], which are the dielectric resonant modes' dipolar momenta. Low energy excitons such as A- and B-excitons oscillate in the long axis direction by coupling with the E_{d1} mode, while high energy excitons C- and E_1-excitons have emission spectra that are polarized along the short axis by coupling to the E_{d2} mode when the dipole mode is energetically close to the exciton modes.

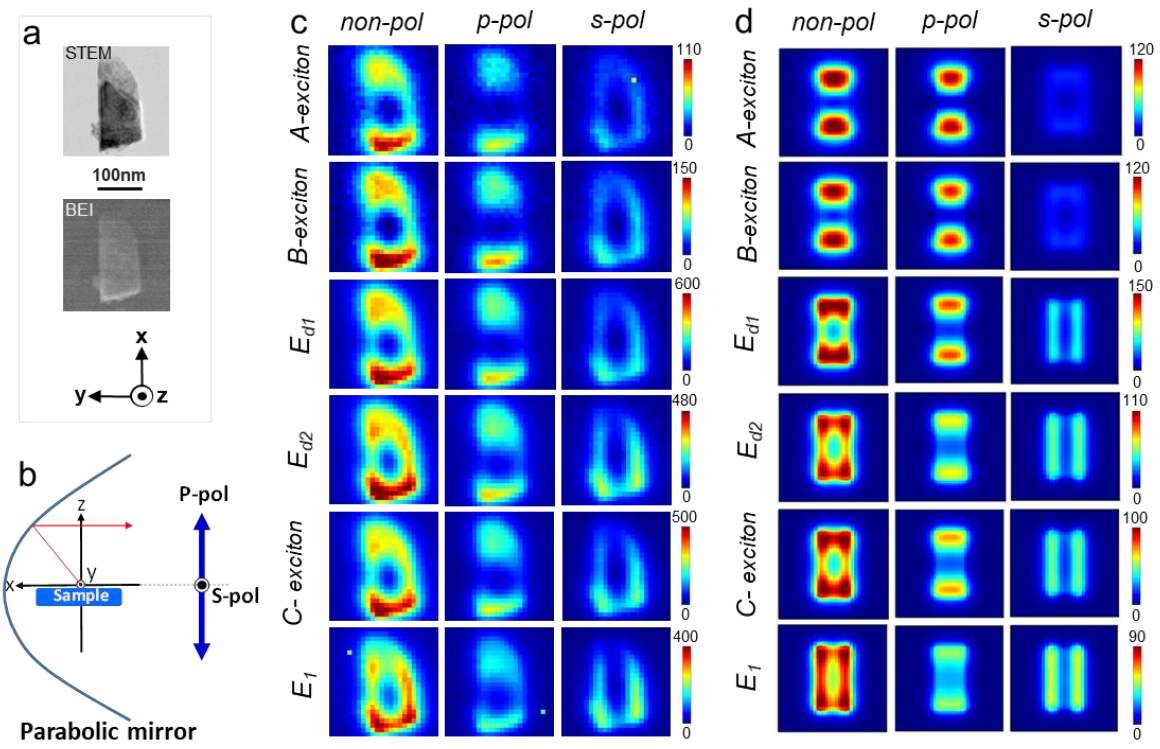

Fig. 5.6: Experiment and BEM simulation CL maps. (a) STEM bright field and BE pictures of a 200 nm by 100 nm rectangular flake. By comparing with coordinate, it is possible to determine the orientation of the sample in the parabolic mirror. (b) A schematic showing the CL system settings. All angles of the CL signal are collected. (c) Experimental CL maps for non-, p-, and s-polarizations, arranged from left to right, without spectral deconvolution. (d) The corresponding BEM simulation for non-, p-, and s-polarizations. CL maps show emissions of the A-exciton, B-exciton, dielectric modes E_{d1} and E_{d2}, C-exciton, and transition energy E_1 in that order, from top to bottom, for both simulation and experiment findings.

5.3.4. Angular spectra patterns

Figure 5.6 presents the angular-energy CL spectra for a rectangular MoS2 flake along the x-z plane with detection angles ranging from 0 to 180°. Figure 5.6a shows the STEM image of the flake. For different electron beam positions, A and B marked by the red squares in the STEM image, the angle-resolved CL spectra are displayed in panel c. Due to shadowing by the sample and sample holder, the signal at = 90° is absent from the angular emission pattern. The emission directionality at 1.84 eV mostly follows to dipole emission patterns, lacking the usual Lambertian shape of the non-coupled incoherent emission, as can be observed in the angle-resolved CL spectra[93]. This implies that the emission process, rather than the excitation process, is connected to the flake dipole mode, because excitation-only enhancement would result in random polarization (usually in-plane for TMDs[95]) in emission without directionality owing to the thermal relaxation process. As demonstrated in Figures 5.6d and e, the BEM simulation with a model flake of similar diameter to the experiment qualitatively reproduces all the experimental data. We should point out that the simulation only considers coherent emission, and hence coherent excitons, depending on the dielectric function of the material.

In the energy range below 3.5 eV, the simulated angular patterns depict the typical emission distributions of an in-plane dipole polarized along the y-axis for excitation point C and a dipole polarized along the x-axis for excitation position D. As a result, this polarization- and angular-dependence finding confirms that excitons are connected to dipoles throughout the emission process, however excitation amplification might still occur because the two excitation processes cannot be differentiated fully in the current experiment.

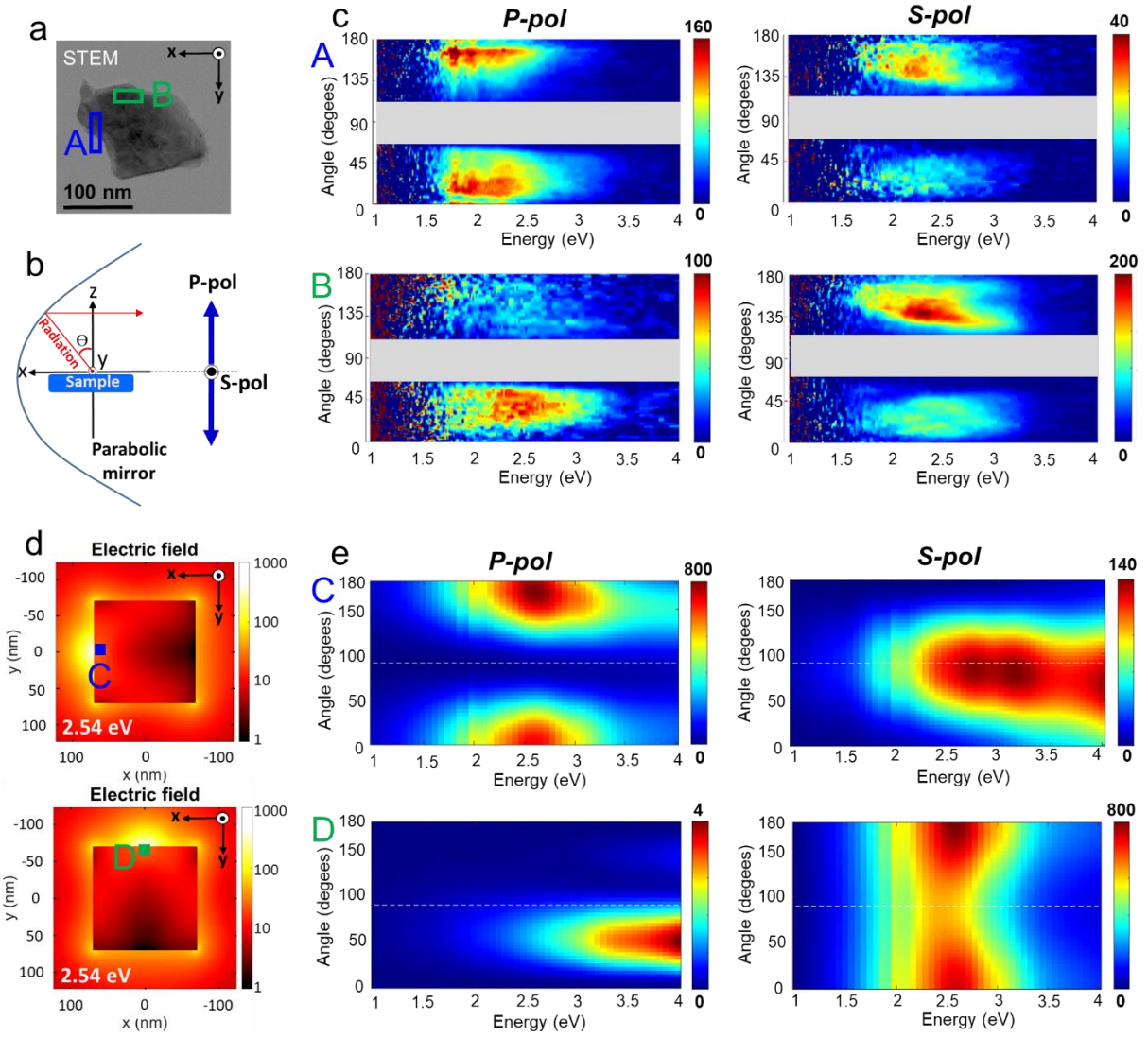

Fig. 5.7: Photon energy and emission angular plots for p and s polarization emissions. (a) STEM bright-field image of a single MoS_2 nanoflake size of ~ 160 nm. (b) A schematic representation of the arrangement for detection. In order to collect the radiated signals at a detection angle spanning from = 0 to 180°, a slit mask parallel to the z-axis must be inserted at y=0. Figure 5a's nanoflake's measured emission angular plots for p- and s- polarization are shown in (c). Due to shadowing from the sample, the plot's gray-hatched region about = 90° is missing. With a beam current of 1.6nA, the measurement is carried out. (d) Calculated time-averaged electric field for two excitation locations C and D on a square flake with a size of 140 nm, obtained at E=2.54 eV. (e) Simulation angle-resolved spectra with p- and s-polarizations for excitation points C and D.

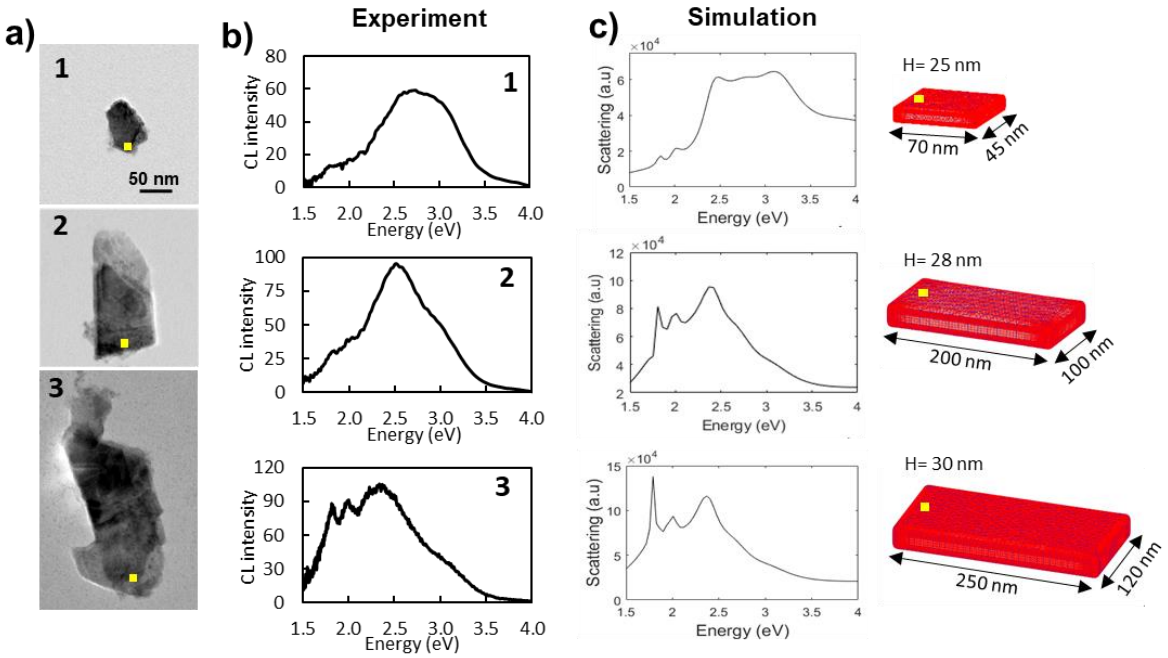

Fig. 5.8: Effect of particle dimensions on CL spectra. a) STEM images of nanoflakes of varied sizes: lateral diameters of (1) 70 nm, (2) 200 nm, and (3) 250 nm. b) Experiment CL spectra of the flakes in panel a's STEM images, with excitation points indicated by yellow square marks. The spectra are acquired by integrating all the emission angles. c) CL spectra simulations and illustrations of corresponding structures with flake size (insets on the right side). The thicknesses of the structures are 25 nm, 28 nm, and 30 nm, respectively. On the structural illustrations, yellow square marks show the locations of the electron beams.

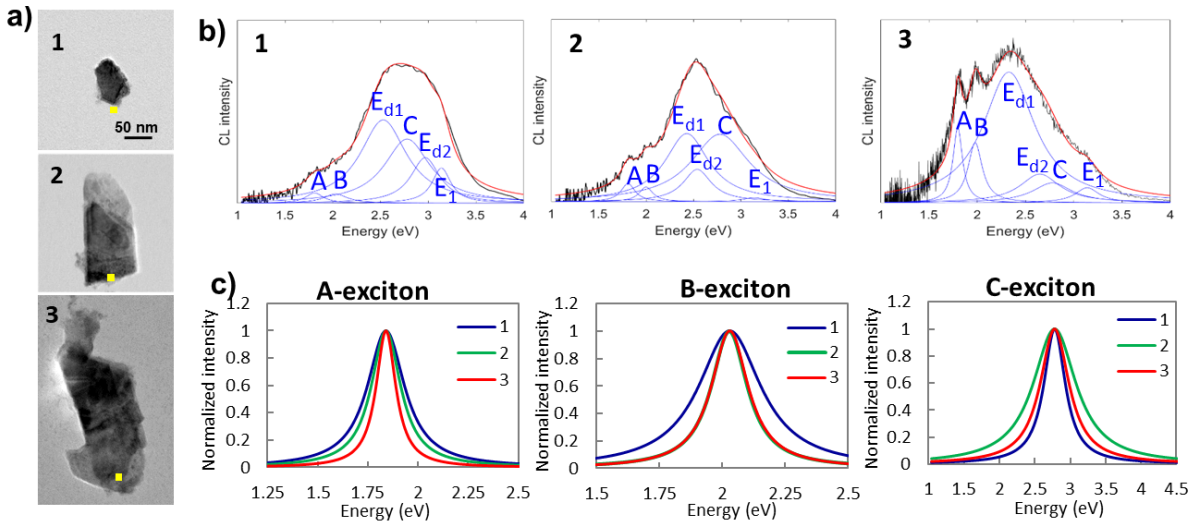

Fig.5.9: Sample size dependence of the line widths of the deconvoluted Lorentzian curves for three exciton emissions. a) STEM images of the measured MoS_2 nanoflakes. b) CL spectra of selected beam spots indicated by yellow square marks in the STEM images in (a). c) Individual A-, B-, and C-exciton emission deconvoluted Lorentzian curves for different samples are presented in (a). As the exciton modes overlap with the dielectric mode (E_{d1} or E_{d2}) resonances, the peak lengths of all the exciton peaks narrow. This variation in peak width might be connected to the exciton-polariton mode line width, which should be examined more thoroughly in future studies.

5.4. Conclusion

Using the CL-STEM method, we were able to visualize the dielectric resonance and exciton emission modes in individual MoS_2 nanoflakes. The data was then examined using spectral deconvolution processing for the CL map data to display the original existence modes separately. The MoS_2 flake exhibits high emissions at E_1=3.1 eV, the C-exciton band at 2.78 eV, and luminescence at lower energies due to the B-exciton band (2.03 eV) and the A-exciton band at (1.84 eV). The energy and density of MoS_2 flakes' dielectric resonance modes are dependent on the morphology of the flakes, and the excitation at the corners and edges of the structures—where the dielectric field hotspots dominate their emission. BEM simulations confirm the electric dipole field distribution and the polarization dependence of the emitted light, demonstrating the coupling between dielectric mode resonance and exciton modes. Furthermore, the angular spectra of the CL emission experimentally indicated the dependency of the emitted field on the emission angle and field polarization with different excitation points using a 4D STEM-CL system. The polarization and angle analyses also support the dielectric and exciton modes interaction. The insights obtained in this chapter on the coupling and enhancement of exciton emission is useful for understanding the light-matter interaction as well as for emitter applications such as single-photon emitters based on TMDs.

Chapter 6- Conclusion and outlook

6.1. General conclusion

In this thesis, two methods to enhance MoS_2 luminescence through optical interaction with nanostructures are presented and the enhancement is nanoscopically using STEM-CL method. Below is a summary of each chapter except Chapter 1- Introduction and Chapter 2- Methods.

Chapter 3: Short-range ordered plasmonic nanoholes

- Using colloidal lithography and film transfer techniques, we fabricate both hexagonal and SRO nanohole arrays.
- By CL photon mapping, we investigated the local field enhancement in SRO holes, where the inter-hole distance varies locally.
- The electric field is mainly concentrated at the hole edges and distributed inhomogeneously among holes.
- The propagation of SPP over randomly oriented holes induces multiple subwavelength interferences that generate Anderson localization of the electromagnetic waves.

Chapter 4: Luminescent enhancement in MoS_2 flakes through coupling with plasmonic resonance

- Fabricate periodic Au nanopyramids using colloidal lithography and film transfer techniques.
- Optical characterization plasmonic Au nanopyramids is investigated through CL and transmission spectral. Plasmonic resonance of nanopyramids measured to be around 2 eV which overlap the A- and B-exciton emissions of MoS_2.
- The hybrid-structure consist of MoS_2 flakes and periodic nanopyramids supported by a thin carbon layer in the bottom.

- Local luminescence enhancement in MoS_2 flake is successfully visualized through CL photon maps, and the enhancement intensity depends on the thickness of MoS_2 flakes

Chapter 5: Exciton-dielectric mode coupling in MoS_2 nanoflakes

- Dielectric resonance and exciton emission modes in single MoS_2 nanoflakes are visualized through the spectral deconvoluted CL maps, to present original existence modes individually.
- MoS_2 flake exhibits the high energy emissions at E_1= 3.1 eV, C-exciton band at 2.78 eV, and the luminescence at lower energies due to B-exciton band (2.03 eV) and A-exciton band at (1.84 eV).
- The energy and number of dielectric resonance modes of MoS_2 flakes depend on the flake shape and size.
- Dielectric field hotspots are located at the corner and the edge of the flake.
- The electric dipole field distribution and the polarization dependence of the emitted light are confirmed by BEM simulations, showing the coupling of dielectric mode resonance and the exciton modes.

6.2. Future work

6.2.1. Distinguish coherent and incoherent CL in the hybrid structure MoS_2-Au nanopyramid by controlling the electron current.

Based on the coherence of the emitted light in regard to the electron beam excitation, the CL signal is categorized into either coherent or incoherent. Coherent electron-induced radiation such as transition radiation, Cherenkov radiation, Smith-Purcell radiation, and surface plasmon–mediated light emission, occur in accordance with the excitation field of the swift electron, therefore, the higher beam current creates proportionally more coherent photons[26][27]. In contrast with the coherent emission, incoherent photon intensity may not be linearly dependent on the beam current, which we can utilize to distinguish the incoherent emission of MoS_2 from the coherent one. The incoherent luminescence processes due to the A and B exciton in MoS_2 can be separated from the coherent transition radiation. The coherent and incoherent emissions can be further identified due to their distinct response to different beam currents. In particular, the incoherent peaks showed saturation of intensity for higher beam currents. From the separation of coherent and incoherent emission in this hybrid structure, it is possible to evaluate how the emission enhancement depends on the excitation current, thereby clarifying the plasmon-exciton coupling mechanism under the electron excitation. Currently, we are conducting a comparison experiment through CL photon maps for the same position MoS_2/Au by different excitation beam currents. By precisely matching the measurement positions between measurements we are analyzing and comparing the ratio of emission peaks for MoS_2, Au and MoS_2/au. However, the comparison needs to be further improved in the future due to factors such as the slight moving of MoS_2 flake on Au nanopyramid array, or the damage of the sample due to high current, leading to changes in physical properties, especially for less durable material MoS_2.

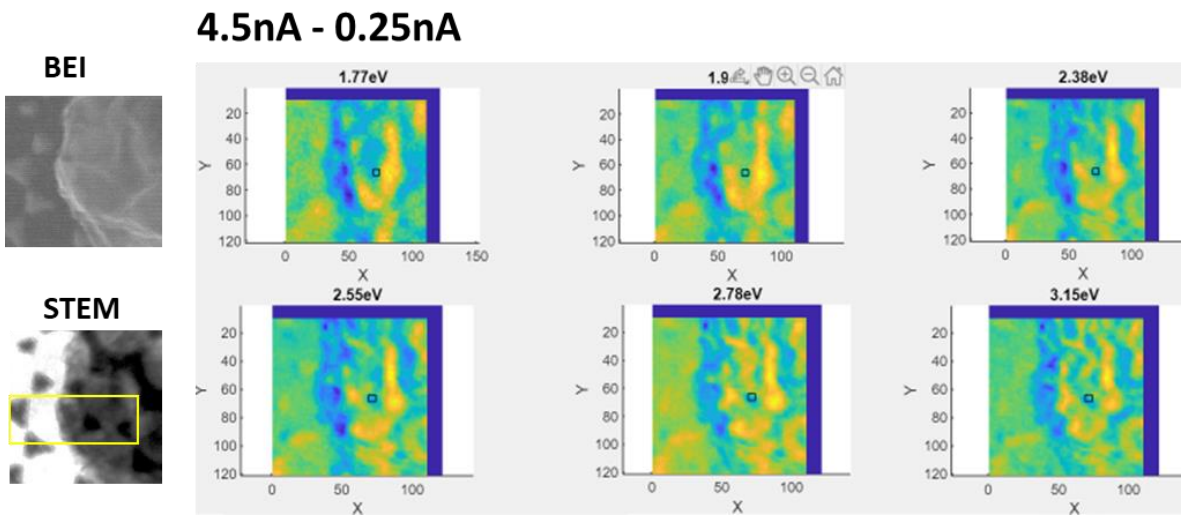

Figure 6.1 Subtraction of CL map at the beam current of 4.5 nA to 0.25 nA with normalized CL intensity.

6.2.2. Tuning the optical emission of MoS_2 by tailoring exciton–plasmon interaction

One of the future works we prioritize is to further evaluate in a more general way the emission enhancement of MoS_2 through the plasmon resonance at different wavelengths. Also using the same fabrication method-colloidal lithography and self-assembly technique, we fabricate plasmonic nanostructures by adjusting the material, and dimension to obtain different resonance wavelengths. Using such plasmonic structures we can enhance emission of MoS_2 at specific emission peaks. For example, as observed in Figure 6.2, the Ag nanoholes with a resonant wavelength of about 500 nm interacted with the C-exciton emission, resulting in higher peak intensity and sharper peak shape. The enhanced emission position in spectrum by the Ag nanostructure has changed compared to the results reported in the above thesis with the

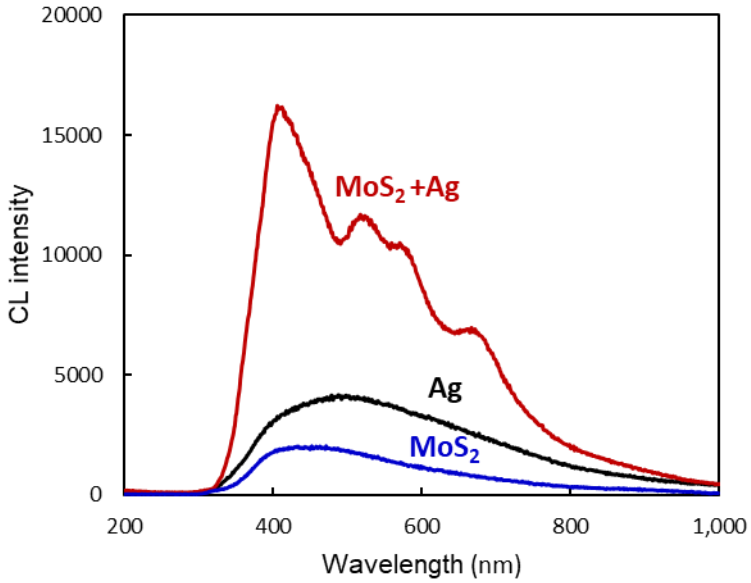

Au pyramids.

Figure 6.2. Luminescence of MoS_2 enhanced by plasmon Ag-nanostructure

References

[1] T. Matsui, A. Agrawal, A. Nahata, and Z. V. Vardeny, “Transmission resonances through aperiodic arrays of subwavelength apertures,” *Nature*, vol. 446, no. 7135, pp. 517–521, 2007, doi: 10.1038/nature05620.

[2] T. Sannomiya, O. Scholder, K. Jefimovs, C. Hafner, and A. B. Dahlin, “Investigation of plasmon resonances in metal films with nanohole arrays for biosensing applications,” *Small*, vol. 7, no. 12, pp. 1653–1663, 2011, doi: 10.1002/smll.201002228.

[3] K. Gu, H. Peng, S. Hua, Y. Qu, and D. Yang, “Plasmon-enhanced blue-light emission of stable perovskite quantum dot membranes,” *Nanomaterials*, vol. 9, no. 5, pp. 1–12, 2019, doi: 10.3390/nano9050770.

[4] Y. Alaverdyan, B. Seplveda, L. Eurenius, E. Olsson, and M. Käll, “Optical antennas based on coupled nanoholes in thin metal films,” *Nat. Phys.*, vol. 3, no. 12, pp. 884–889, 2007, doi: 10.1038/nphys785.

[5] C. Genet, M. P. Van Exter, and J. P. Woerdman, “Fano-type interpretation of red shifts and red tails in hole array transmission spectra,” *Opt. Commun.*, vol. 225, no. 4–6, pp. 331–336, 2003, doi: 10.1016/j.optcom.2003.07.037.

[6] H. Ghaemi, T. Thio, D. Grupp, and T. Ebbesen, “Surface plasmons enhance optical transmission through subwavelength holes,” *Phys. Rev. B - Condens. Matter Mater. Phys.*, vol. 58, no. 11, pp. 6779–6782, 1998, doi: 10.1103/PhysRevB.58.6779.

[7] A. D. Humphrey and W. L. Barnes, “Plasmonic surface lattice resonances on arrays of different lattice symmetry,” *Phys. Rev. B - Condens. Matter Mater. Phys.*, vol. 90, no. 7, pp. 1–8, 2014, doi: 10.1103/PhysRevB.90.075404.

[8] S. Kasani, K. Curtin, and N. Wu, “A review of 2D and 3D plasmonic nanostructure array patterns: Fabrication, light management and sensing applications,” *Nanophotonics*, vol. 8, no. 12, pp. 2065–2089, 2019, doi: 10.1515/nanoph-2019-0158.

[9] C. Cherqui, M. R. Bourgeois, D. Wang, and G. C. Schatz, “Plasmonic Surface Lattice Resonances: Theory and Computation,” *Acc. Chem. Res.*, vol. 52, no. 9, pp. 2548–2558, 2019, doi: 10.1021/acs.accounts.9b00312.

[10] V. G. Kravets, A. V. Kabashin, W. L. Barnes, and A. N. Grigorenko, “Plasmonic Surface Lattice Resonances: A Review of Properties and Applications,” *Chem. Rev.*, vol. 118, no. 12, pp. 5912–5951, 2018, doi: 10.1021/acs.chemrev.8b00243.

[11] S. Golovynskyi *et al.*, “Exciton and trion in few-layer MoS2: Thickness- and temperature-dependent photoluminescence,” *Appl. Surf. Sci.*, vol. 515, no. October 2019, p. 146033, 2020, doi: 10.1016/j.apsusc.2020.146033.

[12] F. Chen, L. Wang, T. Wang, and X. Ji, “Enhanced local photoluminescence of a multilayer MoS_2 nanodot stacked on monolayer MoS_2 flakes,” *Opt. Mater. Express*, vol. 7, no. 4, p. 1365, 2017, doi: 10.1364/ome.7.001365.

[13] J. Theerthagiri, R. A. Senthil, B. Senthilkumar, A. Reddy Polu, J. Madhavan, and M. Ashokkumar, “Recent advances in MoS2 nanostructured materials for energy and environmental applications – A review,” *J. Solid State Chem.*, vol. 252, no. April, pp. 43–71, 2017, doi: 10.1016/j.jssc.2017.04.041.

[14] R. Verre, D. G. Baranov, B. Munkhbat, J. Cuadra, M. Käll, and T. Shegai, “Transition metal dichalcogenide nanodisks as high-index dielectric Mie nanoresonators,” *Nat. Nanotechnol.*, vol. 14, no. 7, pp. 679–683, 2019, doi: 10.1038/s41565-019-0442-x.

[15] A. Splendiani *et al.*, “Emerging photoluminescence in monolayer MoS2,” *Nano Lett.*, vol. 10, no. 4, pp. 1271–1275, 2010, doi: 10.1021/nl903868w.

[16] J. A. Wilson and A. D. Yoffe, “The transition metal dichalcogenides discussion and interpretation of the observed optical, electrical and structural properties,” *Adv. Phys.*, vol. 18, no. 73, pp. 193–335, 1969, doi: 10.1080/00018736900101307.

[17] F. Hu *et al.*, “Imaging exciton-polariton transport in MoSe 2 waveguides,” *Nat. Photonics*, vol. 11, no. 6, pp. 356–360, 2017, doi: 10.1038/nphoton.2017.65.

[18] C. H. Liu *et al.*, “Ultrathin van der Waals Metalenses,” *Nano Lett.*, vol. 18, no. 11, pp. 6961–6966, 2018, doi: 10.1021/acs.nanolett.8b02875.

[19] A. Dasgupta, J. Gao, and X. Yang, “Atomically Thin Nonlinear Transition Metal Dichalcogenide Holograms,” *Nano Lett.*, vol. 19, no. 9, pp. 6511–6516, 2019, doi: 10.1021/acs.nanolett.9b02740.

[20] M. Nauman *et al.*, “Tunable Unidirectional Nonlinear Emission from Transition-Metal-Dichalcogenide Metasurfaces,” *Nat. Commun.*, pp. 1–11, 2021, doi: 10.1038/s41467-021-25717-x.

[21] S. Busschaert, R. Reimann, M. Cavigelli, R. Khelifa, A. Jain, and L. Novotny, “Transition Metal Dichalcogenide Resonators for Second Harmonic Signal Enhancement,” *ACS Photonics*, vol. 7, no. 9, pp. 2482–2488, 2020, doi: 10.1021/acsphotonics.0c00751.

[22] Y. Yang, R. Pan, S. Tian, C. Gu, and J. Li, “Plasmonic hybrids of mos2 and 10-nm nanogap arrays for photoluminescence enhancement,” *Micromachines*, vol. 11, no. 12, pp. 1–12, 2020, doi: 10.3390/mi11121109.

[23] S. Zu, B. Li, Y. Gong, Z. Li, P. M. Ajayan, and Z. Fang, “Active Control of Plasmon–Exciton Coupling in MoS2–Ag Hybrid Nanostructures,” *Adv. Opt. Mater.*, vol. 4, no. 10, pp. 1463–1469, 2016, doi: 10.1002/adom.201600188.

[24] Z. Li *et al.*, “Tailoring MoS2 Exciton-Plasmon Interaction by Optical Spin-Orbit Coupling,” *ACS Nano*, vol. 11, no. 2, pp. 1165–1171, 2017, doi: 10.1021/acsnano.6b06834.

[25] E. Cao, W. Lin, M. Sun, W. Liang, and Y. Song, “Exciton-plasmon coupling interactions: From principle to applications,” *Nanophotonics*, vol. 7, no. 1, pp. 145–167, 2018, doi: 10.1515/nanoph-2017-0059.

[26] B. J. M. Brenny, T. Coenen, and A. Polman, “Quantifying coherent and incoherent cathodoluminescence in semiconductors and metals,” *J. Appl. Phys.*, vol. 115, no. 24, 2014, doi: 10.1063/1.4885426.

[27] F. J. García De Abajo, “Optical excitations in electron microscopy,” *Rev. Mod. Phys.*, vol. 82, no. 1, pp. 209–275, 2010, doi: 10.1103/RevModPhys.82.209.

[28] K. F. Mak and J. Shan, “Photonics and optoelectronics of 2D semiconductor transition metal dichalcogenides,” *Nat. Photonics*, vol. 10, no. 4, pp. 216–226, 2016, doi: 10.1038/nphoton.2015.282.

[29] D. Jariwala, V. K. Sangwan, L. J. Lauhon, T. J. Marks, and M. C. Hersam, “Emerging device applications for semiconducting two-dimensional transition metal dichalcogenides,” *ACS Nano*, vol. 8, no. 2, pp. 1102–1120, 2014, doi: 10.1021/nn500064s.

[30] M. Chhowalla, H. S. Shin, G. Eda, L. J. Li, K. P. Loh, and H. Zhang, “The chemistry of two-dimensional layered transition metal dichalcogenide nanosheets,” *Nat. Chem.*, vol. 5, no. 4, pp. 263–275, 2013, doi: 10.1038/nchem.1589.

[31] Z. Li *et al.*, “Mechanistic insight into the chemical treatments of monolayer transition metal disulfides for photoluminescence enhancement,” *Nat. Commun.*, vol. 12, no. 1, 2021, doi: 10.1038/s41467-021-26340-6.

[32] C. Schwermann *et al.*, “Incorporation of oxygen atoms as a mechanism for photoluminescence enhancement of chemically treated MoS2,” *Phys. Chem. Chem. Phys.*, vol. 20, no. 25, pp. 16918–16923, 2018, doi: 10.1039/c8cp03052a.

[33] Y. Zeng, W. Chen, B. Tang, J. Liao, J. Lou, and Q. Chen, “Synergetic photoluminescence enhancement of monolayer MoS2: Via surface plasmon resonance and defect repair,” *RSC Adv.*, vol. 8, no. 42, pp. 23591–23598, 2018, doi: 10.1039/c8ra03779e.

[34] Y. Dai *et al.*, “Broadband Plasmon-Enhanced Four-Wave Mixing in Monolayer MoS2,” *Nano Lett.*, vol. 21, no. 14, pp. 6321–6327, 2021, doi: 10.1021/acs.nanolett.1c02381.

[35] L. Zhang, R. Gogna, W. Burg, E. Tutuc, and H. Deng, “Photonic-crystal exciton-polaritons in monolayer semiconductors,” *Nat. Commun.*, vol. 9, no. 1, pp. 1–8,

2018, doi: 10.1038/s41467-018-03188-x.

[36] T. Ohno *et al.*, “Hole-size tuning and sensing performance of hexagonal plasmonic nanohole arrays,” *Opt. Mater. Express*, vol. 6, no. 5, p. 1594, 2016, doi: 10.1364/ome.6.001594.

[37] C. Wadell, S. Inagaki, T. Nakamura, J. Shi, Y. Nakamura, and T. Sannomiya, “Nanocuvette: A Functional Ultrathin Liquid Container for Transmission Electron Microscopy,” *ACS Nano*, vol. 11, no. 2, pp. 1264–1272, 2017, doi: 10.1021/acsnano.6b05007.

[38] S. D. Findlay, N. Shibata, H. Sawada, E. Okunishi, Y. Kondo, and Y. Ikuhara, “Dynamics of annular bright field imaging in scanning transmission electron microscopy,” *Ultramicroscopy*, vol. 110, no. 7, pp. 903–923, 2010, doi: 10.1016/j.ultramic.2010.04.004.

[39] F. Sanchez and K. Sobolev, “Nanotechnology in concrete - A review,” *Constr. Build. Mater.*, vol. 24, no. 11, pp. 2060–2071, 2010, doi: 10.1016/j.conbuildmat.2010.03.014.

[40] P. Applications, “Point-of-Care Applications,” pp. 185–203, 2020, doi: 10.1016/j.bios.2019.01.037.NANOHOLE.

[41] S. A. Maier, “Chapter 2 SURFACE PLASMON POLARITONS AT METAL /,” *Plasmon. Fundam. Appl.*, vol. 0, pp. 1–2, 2007.

[42] A. Syahir, “Label-free photonics biosensor transducing nano-biological events,” *J. Biochem. Microbiol. Biotechnol.*, vol. 2, no. 1, pp. 32–38, 2014, doi: 10.54987/jobimb.v2i1.126.

[43] AFMWorkshop, “Measuring and Understanding Force Distance Curves,” vol. 1, no. 888, pp. 4–6, 2020.

[44] F. J. Giessibl, “Advances in atomic force microscopy,” *Rev. Mod. Phys.*, vol. 75, no. 3, pp. 949–983, 2003, doi: 10.1103/RevModPhys.75.949.

[45] G. Zeng, Y. Duan, F. Besenbacher, and M. Dong, “Nanomechanics of Amyloid Materials Studied by Atomic Force Microscopy,” *At. Force Microsc. Investig. into Biol. - From Cell to Protein*, no. March, 2012, doi: 10.5772/36342.

[46] N. Yamamoto, “Development of high-resolution cathodoluminescence system for STEM and application to plasmonic nanostructures,” *Microscopy*, vol. 65, no. 4, pp. 282–295, 2016, doi: 10.1093/jmicro/dfw025.

[47] A. B. Dahlin, “Sensing applications based on plasmonic nanopores: The hole story,” *Analyst*, vol. 140, no. 14, pp. 4748–4759, 2015, doi: 10.1039/c4an02258k.

[48] W. B. Shi *et al.*, “Strong Localization of Surface Plasmon Polaritons with Engineered Disorder,” *Nano Lett.*, vol. 18, no. 3, pp. 1896–1902, 2018, doi:

10.1021/acs.nanolett.7b05191.

[49] Z. Mai *et al.*, “Anderson localization in metallic nanoparticle arrays,” *Opt. Express*, vol. 24, no. 12, p. 13210, 2016, doi: 10.1364/oe.24.013210.

[50] S. J. Kwon *et al.*, “A Plasmonic Platform with Disordered Array of Metal Nanoparticles for Three-Order Enhanced Upconversion Luminescence and Highly Sensitive Near-Infrared Photodetector,” *Adv. Mater.*, vol. 28, no. 36, pp. 7899–7909, 2016, doi: 10.1002/adma.201601680.

[51] M. Balasubrahmaniyam, A. Nahata, and S. Mujumdar, “Anderson localization at the hybridization gap in a plasmonic system,” *Phys. Rev. B*, vol. 98, no. 2, pp. 1–9, 2018, doi: 10.1103/PhysRevB.98.024202.

[52] P. E. Wolf and G. Maret, “Weak localization and coherent backscattering of photons in disordered media,” *Phys. Rev. Lett.*, vol. 55, no. 24, pp. 2696–2699, 1985, doi: 10.1103/PhysRevLett.55.2696.

[53] J. Billy *et al.*, “Direct observation of Anderson localization of matter waves in a controlled disorder,” *Nature*, vol. 453, no. 7197, pp. 891–894, 2008, doi: 10.1038/nature07000.

[54] G. Roati *et al.*, “Anderson localization of a non-interacting Bose-Einstein condensate,” *Nature*, vol. 453, no. 7197, pp. 895–898, 2008, doi: 10.1038/nature07071.

[55] J. Junesch and T. Sannomiya, “Ultrathin suspended nanopores with surface plasmon resonance fabricated by combined colloidal lithography and film transfer,” *ACS Appl. Mater. Interfaces*, vol. 6, no. 9, pp. 6322–6331, 2014, doi: 10.1021/am405443y.

[56] F. Przybilla, C. Genet, and T. W. Ebbesen, “Long vs short-range orders in random subwavelength hole arrays,” *Opt. Express*, vol. 20, no. 4, p. 4697, 2012, doi: 10.1364/oe.20.004697.

[57] M. Kociak and O. Stéphan, “Mapping plasmons at the nanometer scale in an electron microscope,” *Chem. Soc. Rev.*, vol. 43, no. 11, pp. 3865–3883, 2014, doi: 10.1039/c3cs60478k.

[58] D. S. Wiersma, P. Bartolini, A. Lagendijk, and R. Righini, “Localization of light in a disordered medium,” *Nature*, vol. 390, no. 6661, pp. 671–673, 1997, doi: 10.1038/37757.

[59] M. Leonetti, S. Karbasi, A. Mafi, and C. Conti, “Observation of migrating transverse anderson localizations of light in nonlocal media,” *Phys. Rev. Lett.*, vol. 112, no. 19, 2014, doi: 10.1103/PhysRevLett.112.193902.

[60] P. B. Johnson and R. W. Christy, “Optical Constant of the Nobel Metals,” *Phys.*

Rev. B, vol. 6, no. 12, pp. 4370–4379, 1972.

[61] A. Losquin and M. Kociak, "Link between Cathodoluminescence and Electron Energy Loss Spectroscopy and the Radiative and Full Electromagnetic Local Density of States," *ACS Photonics*, vol. 2, no. 11, pp. 1619–1627, 2015, doi: 10.1021/acsphotonics.5b00416.

[62] T. Sannomiya, H. Saito, J. Junesch, and N. Yamamoto, "Coupling of plasmonic nanopore pairs: Facing dipoles attract each other," *Light Sci. Appl.*, vol. 5, no. 9, pp. 1–7, 2016, doi: 10.1038/lsa.2016.146.

[63] N. Yamamoto and T. Suzuki, "Conversion of surface plasmon polaritons to light by a surface step," *Appl. Phys. Lett.*, vol. 93, no. 9, pp. 5–8, 2008, doi: 10.1063/1.2978248.

[64] R. H. RITCHIE, "Plasma Losses by Fast Electrons in Thin Films," *Phys. Rev.*, vol. 106 N.5, no. 5, p. 8, 1956.

[65] E. S. H. Kang, H. Ekinge, and M. P. Jonsson, "Plasmonic fanoholes: on the gradual transition from suppressed to enhanced optical transmission through nanohole arrays in metal films of increasing film thickness," *Opt. Mater. Express*, vol. 9, no. 3, p. 1404, 2019, doi: 10.1364/ome.9.001404.

[66] H. Saito and N. Yamamoto, "Size dependence of bandgaps in a two-dimensional plasmonic crystal with a hexagonal lattice," *Opt. Express*, vol. 23, no. 3, p. 2524, 2015, doi: 10.1364/oe.23.002524.

[67] Y. Ikenoya, M. Susa, J. Shi, Y. Nakamura, A. B. Dahlin, and T. Sannomiya, "Optical resonances in short-range ordered nanoholes in ultrathin aluminum/aluminum nitride multilayers," *J. Phys. Chem. C*, vol. 117, no. 12, pp. 6373–6382, 2013, doi: 10.1021/jp401372k.

[68] J. Prikulis, P. Hanarp, L. Olofsson, D. Sutherland, and M. Käll, "Optical spectroscopy of nanometric holes in thin gold films," *Nano Lett.*, vol. 4, no. 6, pp. 1003–1007, 2004, doi: 10.1021/nl0497171.

[69] D. Y. Lei, J. Li, A. I. Fernandez-Dominguez, H. C. Ong, and S. A. Maier, "Geometry Dependence of Surface Arrays," *ACS Nano*, vol. 4, no. 1, pp. 432–438, 2009.

[70] T. M. Schmidt, M. Frederiksen, V. Bochenkov, and D. S. Sutherland, "Exploring plasmonic coupling in hole-cap arrays," *Beilstein J. Nanotechnol.*, vol. 6, no. 1, pp. 1–10, 2015, doi: 10.3762/bjnano.6.1.

[71] H. Saito, N. Yamamoto, and T. Sannomiya, "Waveguide Bandgap in Crystalline Bandgap Slows Down Surface Plasmon Polariton," *ACS Photonics*, vol. 4, no. 6, pp. 1361–1370, 2017, doi: 10.1021/acsphotonics.6b00943.

[72] H. Saito and N. Yamamoto, “Control of Light Emission by a Plasmonic Crystal Cavity,” *Nano Lett.*, vol. 15, no. 9, pp. 5764–5769, 2015, doi: 10.1021/acs.nanolett.5b01719.

[73] D. Conteduca, I. Barth, G. Pitruzzello, C. P. Reardon, E. R. Martins, and T. F. Krauss, “Dielectric nanohole array metasurface for high-resolution near-field sensing and imaging,” *Nat. Commun.*, vol. 12, no. 1, pp. 1–9, 2021, doi: 10.1038/s41467-021-23357-9.

[74] T. Matsukata, F. J. García de Abajo, and T. Sannomiya, “Chiral Light Emission from a Sphere Revealed by Nanoscale Relative-Phase Mapping,” *ACS Nano*, vol. 15, no. 2, pp. 2219–2228, 2021, doi: 10.1021/acsnano.0c05624.

[75] P. R. Edwards and R. W. Martin, “Cathodoluminescence nano-characterization of semiconductors,” *Semicond. Sci. Technol.*, vol. 26, no. 6, 2011, doi: 10.1088/0268-1242/26/6/064005.

[76] A. Polman, M. Kociak, and F. J. García de Abajo, “Electron-beam spectroscopy for nanophotonics,” *Nat. Mater.*, vol. 18, no. 11, pp. 1158–1171, 2019, doi: 10.1038/s41563-019-0409-1.

[77] H. L. Chen *et al.*, “Determination of n-Type Doping Level in Single GaAs Nanowires by Cathodoluminescence,” *Nano Lett.*, vol. 17, no. 11, pp. 6667–6675, 2017, doi: 10.1021/acs.nanolett.7b02620.

[78] B. G. Yacobi and D. B. Holt, “Cathodoluminescence scanning electron microscopy of semiconductors,” *J. Appl. Phys.*, vol. 59, no. 4, 1986, doi: 10.1063/1.336491.

[79] T. Matsukata, C. Wadell, N. Matthaiakakis, N. Yamamoto, and T. Sannomiya, “Selected Mode Mixing and Interference Visualized within a Single Optical Nanoantenna,” *ACS Photonics*, vol. 5, no. 12, pp. 4986–4992, 2018, doi: 10.1021/acsphotonics.8b01231.

[80] J. Waxenegger, A. Trügler, and U. Hohenester, “Plasmonics simulations with the MNPBEM toolbox: Consideration of substrates and layer structures,” *Comput. Phys. Commun.*, vol. 193, pp. 138–150, 2015, doi: 10.1016/j.cpc.2015.03.023.

[81] N. Matthaiakakis and T. Sannomiya, “Boundary Element Method Simulations of Tunable Chiral Radiation and Active Chirality Switching from Rectangular Graphene Nanosheets: Implications for Dynamic Control of Light Chirality,” *ACS Appl. Nano Mater.*, vol. 3, no. 7, pp. 6816–6826, 2020, doi: 10.1021/acsanm.0c01202.

[82] K. M. McCreary, A. T. Hanbicki, S. V. Sivaram, and B. T. Jonker, “A- and B-exciton photoluminescence intensity ratio as a measure of sample quality for transition metal dichalcogenide monolayers,” *APL Mater.*, vol. 6, no. 11, 2018,

doi: 10.1063/1.5053699.

[83] M. Palummo, M. Bernardi, and J. C. Grossman, “Exciton radiative lifetimes in two-dimensional transition metal dichalcogenides,” *Nano Lett.*, vol. 15, no. 5, pp. 2794–2800, 2015, doi: 10.1021/nl503799t.

[84] D. Y. Qiu, F. H. Da Jornada, and S. G. Louie, “Optical spectrum of MoS2: Many-body effects and diversity of exciton states,” *Phys. Rev. Lett.*, vol. 111, no. 21, pp. 1–5, 2013, doi: 10.1103/PhysRevLett.111.216805.

[85] A. Molina-Sánchez, D. Sangalli, K. Hummer, A. Marini, and L. Wirtz, “Effect of spin-orbit interaction on the optical spectra of single-layer, double-layer, and bulk MoS2,” *Phys. Rev. B - Condens. Matter Mater. Phys.*, vol. 88, no. 4, pp. 1–6, 2013, doi: 10.1103/PhysRevB.88.045412.

[86] V. L. Le, T. J. Kim, H. G. Park, H. T. Nguyen, Y. D. Kim, and H. T. Nguyen, “Temperature dependence of the dielectric function of monolayer MoS2,” *Curr. Appl. Phys.*, vol. 19, no. 2, pp. 182–187, 2019, doi: 10.1016/j.cap.2018.10.007.

[87] L. H. G. Tizei and M. Kociak, “Spectrally and spatially resolved cathodoluminescence of nanodiamonds: Local variations of the NV 0 emission properties,” *Nanotechnology*, vol. 23, no. 17, 2012, doi: 10.1088/0957-4484/23/17/175702.

[88] S. Yanagimoto, N. Yamamoto, T. Sannomiya, and K. Akiba, “Purcell effect of nitrogen-vacancy centers in nanodiamond coupled to propagating and localized surface plasmons revealed by photon-correlation cathodoluminescence,” *Phys. Rev. B*, vol. 103, no. 20, pp. 1–9, 2021, doi: 10.1103/physrevb.103.205418.

[89] M. Taleb, F. Davoodi, F. K. Diekmann, K. Rossnagel, and N. Talebi, “ Charting the Exciton–Polariton Landscape of WSe 2 Thin Flakes by Cathodoluminescence Spectroscopy ,” *Adv. Photonics Res.*, vol. 2100124, p. 2100124, 2021, doi: 10.1002/adpr.202100124.

[90] B. Johns, S. Chattopadhyay, and J. Mitra, “Tailoring Infrared Absorption and Thermal Emission with Ultrathin-film Interferences in Epsilon-Near-Zero Media,” vol. 2100153, pp. 1–9, 2021, doi: 10.1002/adpr.202100153.

[91] U. Hohenester and A. Trügler, “MNPBEM - A Matlab toolbox for the simulation of plasmonic nanoparticles,” *Comput. Phys. Commun.*, vol. 183, no. 2, pp. 370–381, 2012, doi: 10.1016/j.cpc.2011.09.009.

[92] U. Hohenester, “Simulating electron energy loss spectroscopy with the MNPBEM toolbox,” *Comput. Phys. Commun.*, vol. 185, no. 3, pp. 1177–1187, 2014, doi: 10.1016/j.cpc.2013.12.010.

[93] S. Mignuzzi *et al.*, “Energy-Momentum Cathodoluminescence Spectroscopy of Dielectric Nanostructures,” *ACS Photonics*, vol. 5, no. 4, pp. 1381–1387, 2018,

doi: 10.1021/acsphotonics.7b01404.

[94] N. Leisgang *et al.*, “Giant Stark splitting of an exciton in bilayer MoS2,” *Nat. Nanotechnol.*, vol. 15, no. 11, pp. 901–907, 2020, doi: 10.1038/s41565-020-0750-1.

[95] J. A. Schuller *et al.*, “Orientation of luminescent excitons in layered nanomaterials,” *Nat. Nanotechnol.*, vol. 8, no. 4, pp. 271–276, 2013, doi: 10.1038/nnano.2013.20.

Publications and conferences

A. Publications

1. **Dung Thi VU**, Nikolaos Matthaiakakis, Hikaru Saito, Takumi Sannomiya, "Exciton-dielectric mode coup coupling in MoS2 nanoflakes visualized by cathodoluminescence", Nanophotonics 2022; 11(9): 2129–2137.
2. Research**Dung Thi VU**, T. Ohno, N. Yamamoto, T. Sannomiya, "Field localization of hexagonal and short-range ordered plasmonic nanoholes investigated by cathodoluminescence," Journal of Chemical Physics, 152, 074707, 2020.
3. **Dung Thi VU**, Takumi Sannomiya, "Emission enhancement in MoS2 flakes through coupling with plasmonic resonance visualized by cathodoluminescence", in preparation.
4. H. Ohnishi, E. Sabatani, **Dung Thi VU**, S. Yanagimoto, T. Sannomiya, "Highly sensitive pressure and temperature induced SPP resonance shift at gold nanohole arrays," Journal of Chemical Physics,152, 024705, 2020.

B. Oral Presentations

1. Dung Thi VU, Takumi Sannomiya, "Emission enhancement in MoS2 flakes through coupling with plasmonic resonance visualized by cathodoluminescence", 69th JSAP Spring Meeting 2022, March, Kanagawa.
2. Dung Thi VU, Takumi Sannomiya, "Fabrication and optical characterization of SRO plasmonic nanopore by cathodoluminescence", iSPN 2019, November, Kobe.
3. Dung Thi VU, N. Yamamoto, T. Sannomiya, "Optical coupling of short-range ordered nanopores through surface plasmons", 66th JSAP Spring Meeting 2019, March, Tokyo.

C. Poster Presentations

1. Dung Thi VU, Takumi Sannomiya, "Visualization of localized field in single MoS2 nanoflakes by cathodoluminescence", 68th JSAP Spring Meeting 2021, March,

Tokyo.

2. Dung Thi VU, Takumi Sannomiya. “Optical coupling of short-rang-ordered nanopores through surface plasmons”, MRM 2019, December, Yokohama.
3. Dung Thi VU, Takumi Sannomiya, “Electron microscopy observation of biomolecules in nanocuvette”, Kanto Branch of the Japanese Society of Microscopy, March, Tokyo.